Petroleum Research 11 (2026) 712–729

Contents lists available at ScienceDirect

Petroleum Research

journal homepage: http://www.keaipublishing.com/en/journals/petroleum-research/

Full Length Article

Dominant lithofacies and hydrocarbon enrichment characteristics of lacustrine shale reservoirs: A case study of the Qingshankou Formation shale in the Southern Songliao Basin

Jialin Wan [a,*], Lang Liu [a,b,**], Qifeng Jia [a], Mengmeng Liu [a], Zhiyu Fang [a]

[a] School of Energy and Mining Engineering, Xi'an University of Science and Technology, Xi'an 710054, China
[b] Shaanxi Provincial Key Laboratory of Geological Support for Coal Green Exploitation, Xi'an University of Science and Technology, Xi'an 710054, China

ARTICLE INFO

Article history:
Received 3 October 2025
Received in revised form
8 January 2026
Accepted 8 January 2026
Available online 13 January 2026

Keywords:
Pore structure
Enrichment model
Qingshankou Formation
Changling Sag
Songliao Basin

ABSTRACT

With the growing challenges in conventional hydrocarbon exploration, shale oil has emerged as a critical target for future energy supply. The Qingshankou Formation (K_2qn) in the southern Songliao Basin holds significant shale oil potential. However, the complex laminae architecture and poorly constrained lithofacies have hindered a clear understanding of shale oil enrichment mechanisms, thereby limiting efficient exploration and development. This study focuses on the K_2qn shale in the Changling Sag, where a comprehensive characterization of lithofacies and pore structures is carried out using an integrated approach of core description, geochemical analysis, and multi-scale imaging techniques, including thin-section petrography, micro-XRF, MAPS, QEMSCAN, and fluid injection experiments. Three types of argillaceous laminae are identified to reveal significant textural and structural heterogeneity in the shale. Pore systems are dominated by interparticle pores and microfractures, with microfractures playing a crucial role in enhancing pore connectivity and fluid transport. The results also indicate that reservoir quality is jointly controlled by organic matter content, mineral composition, and laminae characteristics. Importantly, two enrichment models are proposed that the layered mixed shale with medium to high organic matter represents a migration-accumulated model influenced by external hydrocarbon input, and the laminated siliceous shale and the mixed shale, both with moderate to high organic content, follow in-situ accumulation patterns dominated by thermal transformation of indigenous organic matter. These findings offer critical geological insights to guide more accurate reservoir prediction and targeted exploration in the lacustrine shale systems.

© 2026 Chinese Petroleum Society. Publishing services by Elsevier B.V. on behalf of KeAi Communications Co. Ltd. This is an open access article under the CC BY-NC-ND license (http://creativecommons.org/licenses/by-nc-nd/4.0/).

1. Introduction

With the rapid depletion of conventional oil and gas resources, the global energy sector faces increasing challenges in meeting growing demand and maintaining long-term supply security. These pressures have prompted many countries to accelerate the exploration and development of unconventional energy resources. Since the early twenty-first century, the shale revolution has reshaped the global energy landscape, particularly in the United States, where commercial-scale shale gas development has demonstrated the transformative potential of unconventional systems (Curtis, 2002; Li et al., 2019; Liu et al., 2022; Zou et al., 2019). In China, crude oil import dependence has exceeded 70 percent, intensifying energy security concerns and elevating unconventional resources, especially shale oil, as strategic priorities for reducing external reliance (Hu et al., 2020; Kuang et al., 2021; Sun et al., 2021; Bai et al., 2024). Estimates indicate that China hosts 3 to 6 billion tons of technically recoverable lacustrine shale oil, demonstrating its considerable exploration potential (Du et al., 2019). Recent exploration breakthroughs across the Ordos (Fu et al., 2020, 2022; Liu et al., 2025), Junggar (He et al., 2023a,b; Tang et al., 2023; Zhi et al., 2019), Bohai Bay (Han et al., 2021; Liu et al., 2023; Pu et al., 2024; Zhao et al., 2022), and Songliao basins (He et al., 2022a; b; Zhang et al., 2023; Wang et al., 2025)

* Corresponding author.
** Corresponding author. School of Energy and Mining Engineering, Xi'an University of Science and Technology, Xi'an 710054, China.
E-mail addresses: JLwan@xust.edu.cn (J. Wan), liulang@xust.edu.cn (L. Liu).
Peer review under the responsibility of Editorial Office of Petroleum Research.

https://doi.org/10.1016/j.ptlrs.2026.01.004
2096-2495/© 2026 Chinese Petroleum Society. Publishing services by Elsevier B.V. on behalf of KeAi Communications Co. Ltd. This is an open access article under the CC BY-NC-ND license (http://creativecommons.org/licenses/by-nc-nd/4.0/).

have advanced understanding of China's lacustrine shale systems and expanded the scope of shale oil development. Among these basins, the Songliao Basin is the largest lacustrine petroliferous basin and contains laterally extensive organic-rich shale intervals deposited within a stable tectono-sedimentary framework (Xiong et al., 2025; Zhang et al., 2022a,b; Zhao et al., 2020). Shale in the basin is characterized by low thermal maturity, high clay mineral content, and strong mineralogical heterogeneity, accompanied by complex pore architectures and pronounced vertical and lateral lithofacies variations (Jin et al., 2021; Ma et al., 2022; Zou et al., 2023).

The Upper Cretaceous Qingshankou Formation (K_2qn) has emerged as a key target due to the widespread development of pure shale oil intervals (Tang et al., 2025). Because shale oil accumulation, mobility, and producibility are governed by micro- to nano-scale pore systems, high-resolution pore structure characterization is essential for evaluating reservoir quality (Huang et al., 2025; Jin et al., 2018; Zheng et al., 2018), understanding fluid transport behavior, and optimizing hydraulic stimulation strategies (Li et al., 2013, 2017, 2018; Lu et al., 2025). Lithofacies analysis provides the geological framework for evaluations because it integrates mineral composition, organic matter enrichment, sedimentary fabric, and reservoir space features (Feng et al., 2024; He et al., 2025; Wan et al., 2025). Moreover, many research has emphasized the critical influence of laminae heterogeneity on shale reservoir behavior. Laminated shales generally exhibit higher hydrocarbon generation potential and more favorable reservoir properties than massive mudstones, underscoring the importance of laminae-controlled variations in oil storage, retention, and production performance (Yawar and Schieber, 2017; Lin et al., 2017; Hua et al., 2021). Within the Qingshankou Formation, diverse architectures have been recognized, including layered, laminated and massive units (Pang et al., 2023a,b). Additional studies have revealed the presence of clay mineral, felsic silt, and ostracod laminae, which occur individually or as mixed assemblages (Sun et al., 2024). The mineralogical and diagenetic complexity of these laminae is further reflected in the subdivision of ostracod laminae into calcareous, pyritic, and fragmental types (Hua et al., 2022). Through integrated core observations, thin-section petrography, XRD, elemental geochemistry, and advanced logging, researchers have constructed refined vertical facies frameworks and proposed multiple lithofacies classification schemes (Liu et al., 2018; Pang et al., 2023a,b). These studies demonstrate that high-organic and medium-organic laminated shales constitute the principal enrichment facies for hydrocarbon accumulation, and laminated felsic shales commonly develop pore fracture systems that support oil sustained production (Liu et al., 2021). Complementary enrichment models exhibit distinct pore structures, movable oil content, and fracturing responses.

Shale oil exploration in the Songliao Basin has expanded southward, highlighting the Changling Sag and the Lishu Fault Depression as promising frontier areas (Zhang et al., 2022a,b; Li et al., 2024; Xiao et al., 2025). The high-yield industrial shale oil flow from the Well JY 1HF within the Qingshankou Formation further confirms the significant resource potential of these intervals (Zhang et al., 2020). However, substantial heterogeneity in depositional architecture and laminae composition continues to limit the establishment of a unified lithofacies classification system and constrains a comprehensive understanding of pore scale heterogeneity and its influence on shale oil enrichment. Previous studies have largely focused on macroscopic reservoir characteristics, whereas high-precision pore structure characterization and lithofacies-controlled enrichment mechanisms have received insufficient attention. Therefore, this study conducts an integrated pore structure investigation across representative lithofacies of the K_2qn shale in the Changling Sag. By combining thin-section petrography, scanning electron microscopy, fluid injection tests, quantitative grain fluorescence analysis, comprehensive geochemical and reservoir characterization, this work reveals the shale lithofacies controls on pore heterogeneity and clarifies the mechanisms of hydrocarbon enrichment. The results establish a geological framework for identifying favorable shale lithofacies and support the optimized exploration and development of lacustrine shale oil.

2. Samples and methods

2.1. Samples

The K_2qn shale in the Changling Sag is influenced by a warm and humid climate combined with extensive lacustrine transgressions, leading to thick accumulations of fine-grained sedimentary rocks enriched in organic matter (Bai et al., 2024; Wang et al., 2024). The study focuses on three wells aligned from north to south as Wells X1, X2, and X3 (Fig. 1). The investigated intervals correspond to the first and second members of the K_2qn shale (Fig. 2), with sampling depths of 2298.65–2446.71 m for Well X1, 2216.11–2372.00 m for Well X2, and 2325.16–2462.41 m for Well X3. Considering core preservation quality and sampling conditions, a total of 200 core samples were collected from wells X1 and X3. These cores were obtained using pressurized, sealed coring techniques and stored at low temperatures to preserve their integrity for subsequent experimental analyses. Additionally, 62 core samples from Well X2 were sourced from the Jilin Oilfield Core Repository.

2.2. Experiments

To systematically elucidate the pore structure and shale oil enrichment characteristics of the K_2qn shale, the experimental methodology focused on three main aspects. (i) Shale lithofacies types were systematically classified through integrated organic geochemical testing, mineralogical composition analysis, and thin section petrography. (ii) Specific properties of pore structure within different shale lithofacies were comprehensively characterized by combining scanning electron microscopy (SEM) with reservoir fluid injection experiments, supported by high-resolution image analysis of modular automated processing systems (MAPS) applied to various laminae structures. (iii) Shale reservoir hydrocarbon content was evaluated through quantitative fluorescence and movable oil assessment techniques, ultimately leading to the development of a crude oil enrichment model for favorable lithofacies.

2.2.1. Total organic carbon measurement and rock pyrolysis analysis

Shale samples finer than 100 mesh were selected and pretreated with dilute hydrochloric acid to remove carbonate minerals. The total organic carbon (TOC) content was determined using a LECO CS230 carbon-sulfur analyzer, following the Chinese national standard of GB/T 19145-2003 determination of total organic carbon in sedimentary rocks. Rock pyrolysis analysis was performed using a Rock-Eval® 6 instrument in accordance with GB/T 18602-2012 rock pyrolysis analysis. Approximately 100 mg of powdered sample was subjected to pyrolysis under an inert atmosphere. Volatile hydrocarbon content (S_1) was measured during isothermal heating at 300 °C for 3 min. Subsequently, the temperature was increased at a rate of 25 °C/min to 650 °C to quantify the pyrolysable hydrocarbon content (S_2) within the 300–650 °C range. The maximum pyrolysis temperature (Tmax) was recorded

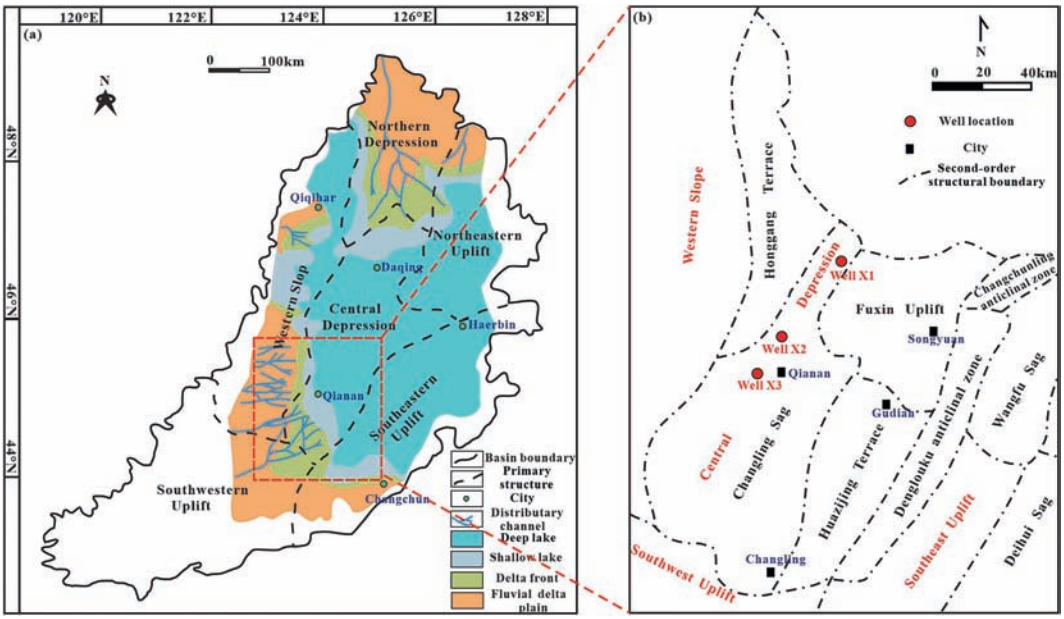


Fig. 1. Location and geological setting of shale oil wells targeting the K_2qn shale in the Changling Sag, Southern Songliao Basin. (a) Regional location of the study area; (b) Structural divisions and sedimentary facies distribution of the Songliao Basin (modified from Zhang et al. (2020)); (c) Distribution of wells X1, X2, and X3.

as an indicator of the thermal maturity of the organic matter.

2.2.2. X-ray diffraction (XRD) analysis

The mineralogical composition of shale samples was analyzed using a Rigaku D/Max-2500 X-ray diffractometer manufactured by Rigaku Corporation in Japan. Approximately 10 g of powdered sample with a particle size of 200 mesh were prepared for bulk mineral analysis. The instrument was operated at an accelerating voltage of 45 kV and a current of 150 mA. The scanning range was set from 2.6° to 45°, with a scanning speed of 2° per minute and a step size of 0.02°. For clay mineral analysis, samples were pretreated with 0.3 M acetic acid and 10 percent hydrogen peroxide to remove carbonate and organic matter. Clay-sized particles were then separated using the suspension-settling method. Oriented specimens were prepared on glass slides for further analysis. The identification and semiquantitative evaluation of clay and common non-clay minerals were conducted in accordance with the Chinese industry standard SY/T 5163-2018 XRD analytical methods for clay minerals and common non-clay minerals in sedimentary rocks.

2.2.3. Thin sections analysis

Rock core samples were cut perpendicular to bedding to prepare standard thin sections. Mineral distribution and laminae structures were identified under plane- and cross-polarized light using a Nikon 80i microscope. High-resolution full-section images were acquired via a digital imaging system for comprehensive documentation. Elemental analysis was then conducted using a Bruker M4 TORNADO micro-XRF spectrometer. Operating at 50 kV and 800 μA, with the detector maintained at −44.9 °C, the instrument performed raster scanning at a 20 μm step size. Elemental mapping focused on major components such as silicon (Si), sodium (Na), potassium (K), calcium (Ca), magnesium (Mg), and aluminum (Al), aiming to reveal their spatial distribution within the shale matrix.

2.2.4. SEM observation and MAPS imaging

Shale samples were sectioned perpendicular to the bedding into standardized blocks (1 cm × 1 cm × 2 mm), followed by surface polishing using a Leica argon ion milling system to produce ultra-smooth surfaces and reduce topographic artifacts for high-resolution SEM imaging. Following carbon coating, high-resolution imaging of laminated regions was conducted using an FEI Apreo field emission scanning electron microscope (FE-SEM) under high vacuum conditions (<60 Pa). The microscope operated at an accelerating voltage of 2 kV and a working distance of 4.0 mm, with imaging parameters adjusted between 10 and 15 kV to enhance surface contrast and resolution. Then, high-resolution, large-area images (spatial resolution >10 nm) were acquired using the MAPS technology under optimized conditions of 5 kV accelerating voltage, 0.4 nA beam current, 4 mm working distance, and a scanning step size of 20 μm. Subsequently, microscale mineralogical mapping over a 1 cm × 1 cm region was performed using the FE-SEM equipped with a QEMSCAN system. Image analysis was conducted via the Edge Threshold Auto-Processing (ETAP) technique, which included grayscale segmentation, identification of organic and inorganic pores, and superimposition of mineral maps onto grayscale images. This allowed for quantitative classification of pore types, including intraparticle pores, interparticle pores, intercrystalline pores, and microfractures.

2.2.5. Fluid injection methods

A combined experimental approach using low-temperature nitrogen adsorption (LTNA) and mercury injection capillary pressure (MICP) was applied to comprehensively characterize pore size distributions in shale reservoirs. For LTNA test, shale samples were ground to 60–80 mesh and pretreated with solvents to remove free hydrocarbons and impurities. Samples were then degassed under vacuum at 80 °C for 8 h to eliminate moisture and volatiles. Adsorption measurements were conducted at 77 K using an Autosorb-IQ-MP surface area and porosity analyzer. Nitrogen adsorption data were collected over a relative pressure range of 0.01–0.995, and pore size distributions were calculated using Density Functional Theory (DFT) models. For MICP test, samples were cut into smooth cubes perpendicular to bedding and analyzed with an AutoPore 9500 mercury intrusion porosimeter. Testing conditions included a contact angle of 130°, mercury

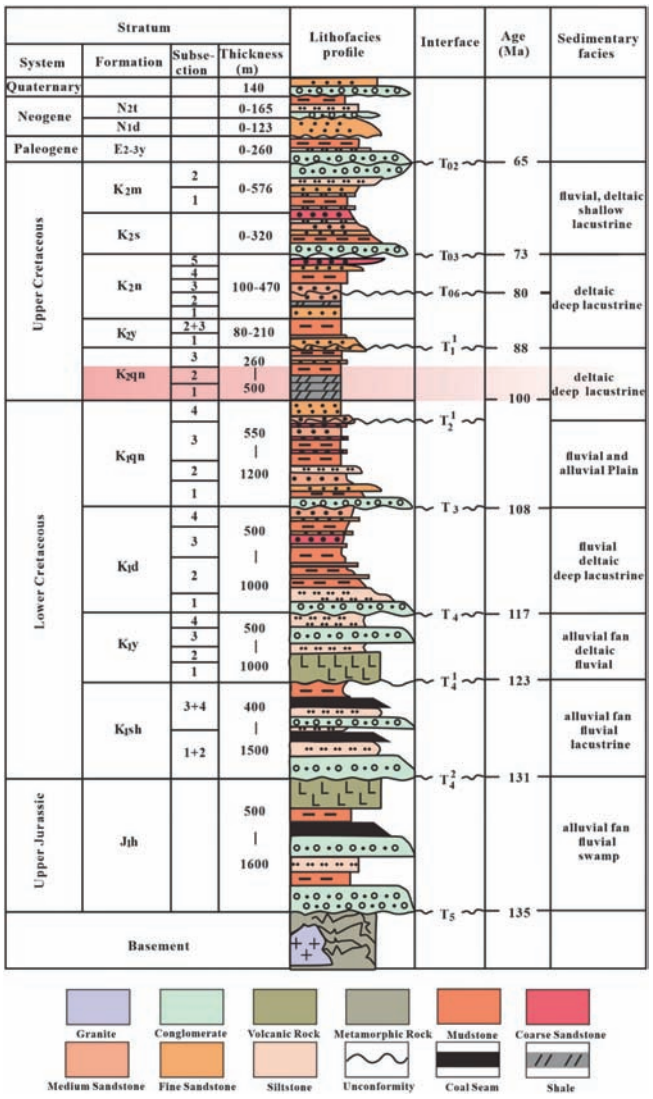


Fig. 2. Comprehensive strata histogram of K_2qn shale in the Changling Sag.

surface tension of 485 dyn/cm, and pressures ranging from 0.2 to 30000 psi, with a 1-min equilibration time per step. Pore throat radii and cumulative pore volumes were derived from mercury intrusion data using the Washburn equation.

2.2.6. Quantitative fluorescence technique

Quantitative Grain Fluorescence on Extracts (QGF-E) and Total Scanning Fluorescence (TSF) were essential spectroscopic methods used to assess hydrocarbon occurrence states within shale reservoirs. In this study, about 0.1 g of shale powder (80–100 mesh) was extracted with 20 mL dichloromethane via two cycles of ultrasonic treatment to remove surface-adsorbed hydrocarbons. The supernatant was analyzed using a Varian Cary-Eclipse fluorometer. To minimize fluorescence quenching, QGF-E measurements were prioritized. Key metrics included normalized fluorescence intensity and maximum emission wavelength (λ_{max}). TSF parameters comprised maximum fluorescence intensity (TSF-Max), and the parameters of R_1 and R_2 were additionally utilized to distinguish compositional and maturity variations in shale oil.

All experimental procedures were conducted at the Experimental Center of the Research Institute of Petroleum Exploration and Development (RIPED), PetroChina. The experiments were implemented in strict compliance with standardized operational protocols and rigorous quality control procedures, thereby ensuring the accuracy, reliability, and reproducibility of the acquired data.

3. Results

3.1. Geochemistry and mineralogy

The K_2qn shales are characterized by relatively high organic matter abundance, with TOC values ranging from 0.32% to 4.48% (Fig. 3a). Notably, over 92% of the samples exhibit TOC values exceeding 1%, providing a substantial organic matter basis for hydrocarbon generation. The hydrocarbon generation potential (S_1+S_2) varies between 0.51 mg/g and 19.96 mg/g, averaging 10.05 mg/g (Fig. 3b). Approximately 88% of samples have values above 6 mg/g, indicating strong hydrocarbon-generating potential. According to the evaluation diagrams proposed by Peters (1986) and Peters and Cassa (1994), the TOC and S_2 values for these shales fall within the good to very good source rock categories (Fig. 3c). Comparative analysis among the analyzed wells reveals distinct generative capacities. The samples from Well X1 shows TOC values between 2% and 3%, and a corresponding S_1+S_2 averaging 11.21 mg/g, reflecting a favorable generation potential. The samples from Well X2 exhibits a slightly lower average TOC of 1.77% and an S_1+S_2 mean value of 9.24 mg/g. Besides, samples from Well X3 presents the lowest organic richness, with an average TOC of 1.65% and S_1+S_2 of 8.82 mg/g. The Tmax-HI cross-plot results indicate that the organic matter is primarily type II kerogen, mainly derived from lacustrine algae and plankton, with minor contributions from type I kerogen (Fig. 3d). Tmax values predominantly range from 420 °C to 460 °C, indicating that the organic matter is at a low to moderate maturity stage, corresponding to early to peak oil generation. It is noteworthy that several samples from Well X1 exhibit suppressed Tmax values, which may result from thermal alteration of retained hydrocarbons.

Mineralogical analysis indicates that the shale is primarily composed of clay minerals (10.5%~61.8%), quartz (20.8%~46.0%), feldspar (6.2%~25.4%), and carbonates (0~28.2%). Moreover, samples from Well X1 exhibit higher average clay mineral and quartz contents. Illite and illite-smectite mixed layers are the dominant types, with Well X1 showing a notably high illite content (Fig. 4). In contrast, samples from Wells X2 and X3 contain more illite-smectite mixed-layer, reflecting a lower degree of diagenetic transformation. Based on the above experimental results, 37 representative samples are selected for subsequent analyses (Table 1).

3.2. Laminae classification and attributes

Based on the criterion of the dominant component exceeding 50%, four types of laminae are identified in the K_2qn shale (Fig. 5): argillaceous laminae (AL), silt laminae (SL), carbonate laminae (CL), and mixed laminae (ML). Different types of laminae exhibit distinct mineralogical characteristics. AL are the most widespread and typically appear brown, gray, or dark gray, mainly consisting of cryptocrystalline or platy clay minerals (Fig. 5a). Under microscopic observation, fine-silt-sized quartz and feldspar grains are sub-rounded to sub-angular, either dispersed or aligned along the bedding plane (Fig. 5b), and occasionally form localized aggregates (Fig. 5c). Carbonate particles show similar spatial arrangements. During diagenesis, AL commonly undergo plastic deformation and localized liquefaction, resulting in liquefaction veins accompanied by grain reorganization and mineral concentration (Fig. 5d). SL occur less frequently and are thinner compared to AL, exhibiting

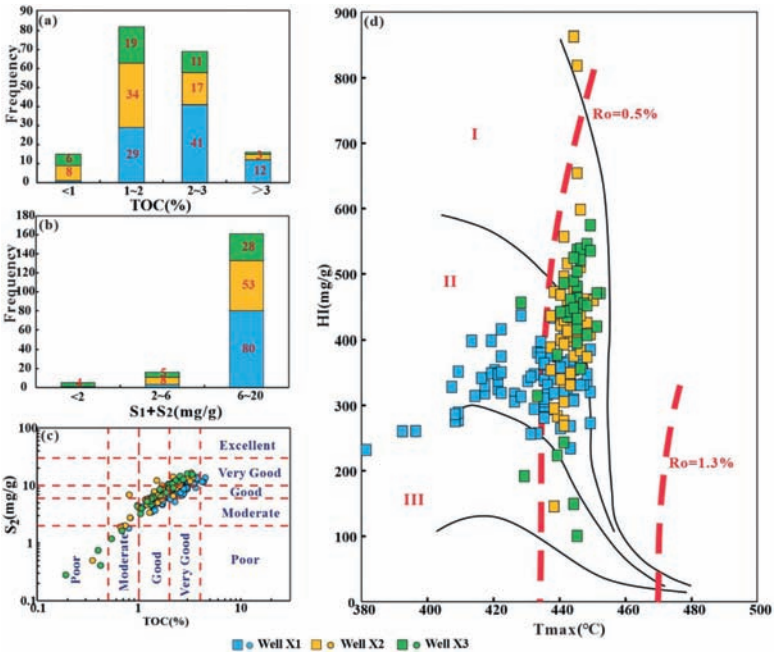


Fig. 3. Abundance and kerogen type distribution characteristics of organic matter in the K_2qn shale. (a) TOC frequency distribution histogram; (b) S_1+S_2 frequency distribution histogram; (c) TOC-S2 cross-lot; (d) Tmax-HI cross-lot.

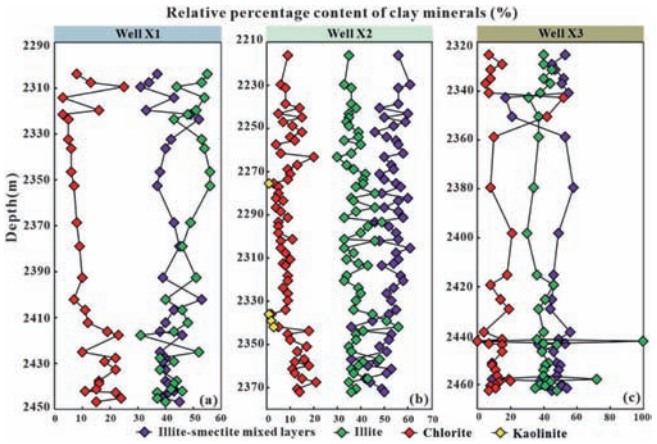


Fig. 4. Clay mineral distribution characteristics of the K_2qn shale in the Changling Sag. (a) Well X1; (b) Well X2; (c) Well X3.

gray-white to white under plane-polarized light and displaying first-order interference colors under cross-polarized light (Fig. 5e and f). They typically form banded, lenticular, or wavy structures and are often interbedded with AL or CL, with sharply defined boundaries that indicate variations in depositional energy. CL develop at moderate frequencies and primarily consist of directionally aligned bioclastic debris dominated by calcite, alongside minor amounts of quartz, feldspar, and clay minerals (Fig. 5g). These laminae display relatively good lateral continuity, although lenticular and discontinuous geometries also occur, reflecting episodic biogenic inputs and fluctuating hydrodynamic conditions. ML exhibit complex grain-size distributions and mineralogical compositions, often forming under fluctuating hydrodynamic conditions or from mixed sediment sources (Fig. 5h). Their heterogeneity reflects transitional depositional environments and signals variations in energy levels or sediment supply during shale formation.

In natural geological settings, shales typically comprise vertically stacked, alternating laminae types that form genetically related depositional sequences. In this study, the 1 cm thickness threshold is used to classify shale structures into layered and laminated categories. Further subdivision reveals three sedimentary assemblages: ①the argillaceous layered assemblage, dominated by fine-grained clay minerals with a compact structure and subdivided into homogeneous, disturbed, and clastic-bearing subtypes; ②the interbedded laminae assemblage, consisting of alternating AL, SL, and CL; ③ and the mixed laminae assemblage, characterized by a uniform mixture of various mineral components within the laminae.

3.3. Classification and characteristics of shale lithofacies

The classification of shale lithofacies aims to achieve high-resolution correlations, which are essential for the effective evaluation and exploration of shale hydrocarbon resources (Zou et al., 2015). In this study, the K_2qn shale lithofacies are classified through an integrated analysis of geochemical characteristics, mineralogical composition, and sedimentary structures. Firstly, the bulk mineral composition of the shale samples is quantitatively classified using a mineral triad classification system (Wu et al., 2021). Then, organic matter abundance is categorized based on the relationship between HI and TOC, resulting in three classifications: low (TOC<1%), medium (1% $\leq$ TOC$\leq$2%), and high (TOC>2%) (Liu et al., 2018). Guided by the principles of practicality and operability, six lithofacies types within the K_2qn shale are identified using an integrated classification scheme that considers TOC, mineralogical composition, and sedimentary structural characteristics. These types are: massive shale with medium to high organic matter (I), layered siliceous shale with medium to high organic matter (II), layered mixed shale with medium to high organic matter (III), layered clayed shale with medium to high organic matter (IV), laminated siliceous shale with medium

Table 1
The geochemical characteristics and mineral composition of K_2qn shale.

Well	Sample No.	Depth (m)	TOC (%)	Mineral composition content (%)					
				Clay	Quartz	K-feldspar	Plagioclase	Carbonate	Pyrite
X1	X1-1	2304.69	2.44	42.3	26.3	0.9	17.4	9.7	3.4
	X1-2	2310.96	1.62	37.1	30.8	0.7	14.5	14.1	2.8
	X1-3	2317.34	1.74	34.1	34.7	0.5	21.9	2.6	6.2
	X1-4	2332.29	1.57	32.3	25.9	1.6	11.1	23.7	5.4
	X1-5	2410.15	2.94	48.4	28.7	1.0	10.5	7.9	3.5
	X1-6	2415.78	2.45	54.1	27.9	0.0	8.7	5.8	3.5
	X1-7	2419.59	1.89	44.5	34.5	0.5	10.1	9.3	1.1
	X1-8	2425.62	2.93	44.4	29.4	0.8	11.4	13.1	0.9
	X1-9	2430.68	2.68	40.3	43.3	0.9	8.9	3.5	3.1
	X1-10	2437.14	2.00	41.7	37.2	0.5	10.4	9.9	0.3
	X1-11	2443.26	2.66	44.0	36.0	0.3	7.3	7.4	5.0
	X1-12	2446.13	2.95	42.1	38.2	0.8	8.5	7.1	3.3
X2	X2-1	2240.48	1.95	38.9	33.4	3.1	18.7	2.8	3.1
	X2-2	2248.80	1.78	37.4	29.0	1.2	14.3	14.4	3.7
	X2-3	2253.95	2.10	41.4	36.2	1.3	13.8	4.4	2.9
	X2-4	2261.48	1.15	47.4	27.2	0.8	9.6	11.3	3.7
	X2-5	2266.90	1.80	31.3	33.3	1.3	20.4	8.5	5.2
	X2-6	2275.43	0.80	39.9	37.2	1.0	11.2	6.1	4.6
	X2-7	2301.29	3.27	41.1	20.8	0.6	24.0	10.4	3.1
	X2-8	2318.14	2.32	49.6	27.9	1.0	13.0	4.9	3.6
	X2-9	2323.75	1.53	53.2	24.5	1.3	9.3	9.7	2.0
	X2-10	2336.01	1.83	42.7	33.2	1.1	10.0	8.4	4.6
	X2-11	2343.76	2.75	38.4	34.3	1.5	11.6	11.9	2.3
	X2-12	2351.00	1.20	43.0	33.5	1.0	15.0	5.0	2.5
	X2-13	2356.89	2.33	46.2	29.1	1.3	7.1	14.4	1.9
	X2-14	2359.83	2.53	53.3	34.3	0.9	7.2	2.1	2.2
	X2-15	2363.30	1.91	42.5	33.9	1.3	12.9	6.9	2.5
	X2-16	2367.45	3.19	51.0	32.5	0.6	10.8	4.8	0.3
X3	X3-1	2331.23	1.93	34.7	36.8	3.1	13.7	9.5	2.2
	X3-2	2398.08	1.98	46.1	24.7	2.0	14.0	9.6	3.6
	X3-3	2429.14	1.39	33.7	29.9	2.4	16.7	14.7	2.6
	X3-4	2441.50	2.54	42.6	29.7	2	12.4	13	0.3
	X3-5	2443.62	2.30	36.9	27.7	1.3	13.3	17.7	3.1
	X3-6	2446.50	2.13	38.4	27.1	1.5	22.2	6.1	4.7
	X3-7	2451.21	1.94	44.4	24.9	1.1	9.8	16.1	3.7
	X3-8	2457.85	0.68	48.4	26.8	2.2	14.2	8.1	0.3
	X3-9	2460.48	1.87	55.4	24.8	1.6	11.3	3.5	3.4

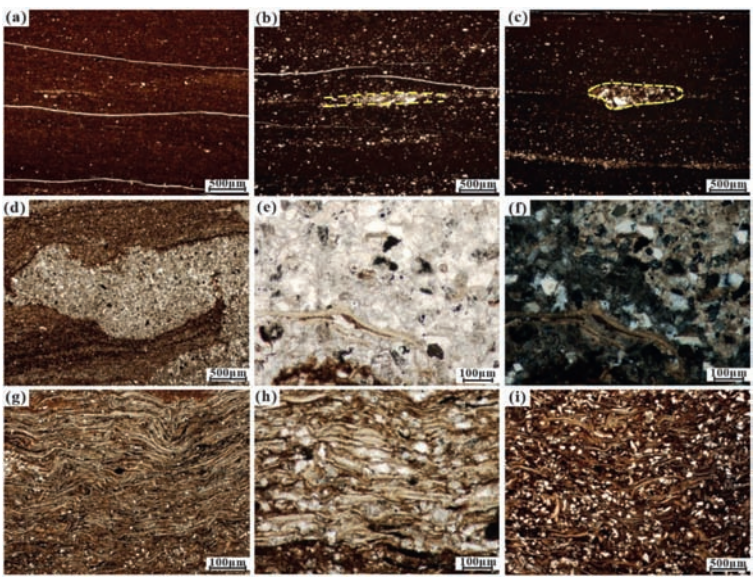


Fig. 5. Mineralogical characteristics of sedimentary structures in the K_2qn shale under optical microscopy. (a) Homogeneous argillaceous fabric formed by >90% oriented clay minerals, sample X1-5; (b) Discontinuous, horizontally aligned felsic laminae among argillaceous matrix, sample X1-11; (c) Aggregated felsic clasts forming lenticular structures in argillaceous matrix, sample X2-16; (d) Liquefaction veins developed within argillaceous fabric, sample X3-4; (e–f) Mineral distribution and color features of silt laminae, sample X2-5; (g) Densely packed shell within bioclastic laminae, sample X3-5; (h) Stratified bioclasts with interparticle felsic infilling, sample X2-5; (i) Mineralogical distribution within mixed laminae, sample X2-11.

organic matter (V) and laminated mixed shale with medium to high organic matter (VI) (Fig. 6). It should be noted that the layered structure of the K_2qn shale is predominantly argillaceous layer. Specifically, based on thin-section observations, the III lithofacies are further subdivided into homogeneous argillaceous layer (III_1), disturbed layer (III_2), and clastic layer (III_3). It is important to note that shale lithofacies with low organic matter content are sparsely distributed and have been excluded from the main classification framework presented in this study.

Type I lithofacies exhibit relatively higher organic matter abundance, with an average TOC of approximately 2.05%. The lithofacies are characterized by consistent color, grain size, and mineralogical composition. Clay minerals dominate in the shale, comprising 38.4%–46.1%, and feldspar and quartz together contribute 40.0%–50.0%. Carbonate minerals are generally present in amounts below 10.0%.

In contrast, type II lithofacies primarily consist of argillaceous layers, which display a uniform dark coloration under microscopic examination. The TOC values range from 1.90% to 3.00%, and the clay mineral content averages 38.8%. Feldspar and quartz concentrations are higher than that in type I shale lithofacies, averaging 53.3%. A representative sample X2-3 reveals enrichment of Si and Al, accompanied by elevated Fe content, reaching up to 4.30%.

Type III lithofacies are predominantly composed of argillaceous layers, exhibiting notable heterogeneity. The III_1 lithofacies show an average TOC of 2.66%, with clay mineral content ranging from 41.1% to 48.4%, and feldspar concentrations varying from 40.2% to 48.1%. Thin-section analysis of sample X1-5 reveals a typical argillaceous layered fabric with uniform coloration. Elemental analysis indicates dominant Si content (60.30%), followed by Al (19.66%) and K at 7.60%. The III_2 lithofacies are marked by the presence of liquefied sand veins, showing significant variability in microscopic morphology across samples. TOC values range from 1.20% to 2.66%, with clay mineral content between 32.3% and 46.2%, feldspar from 37.5% to 49.5%, and elevated carbonate content up to 23.7%. The liquefaction veins in sample X1-11 are arranged in a planar pattern, roughly parallel to the bedding planes, indicating fluctuating fluid pressures during diagenesis or external disturbances. Elemental mapping highlights substantial Si

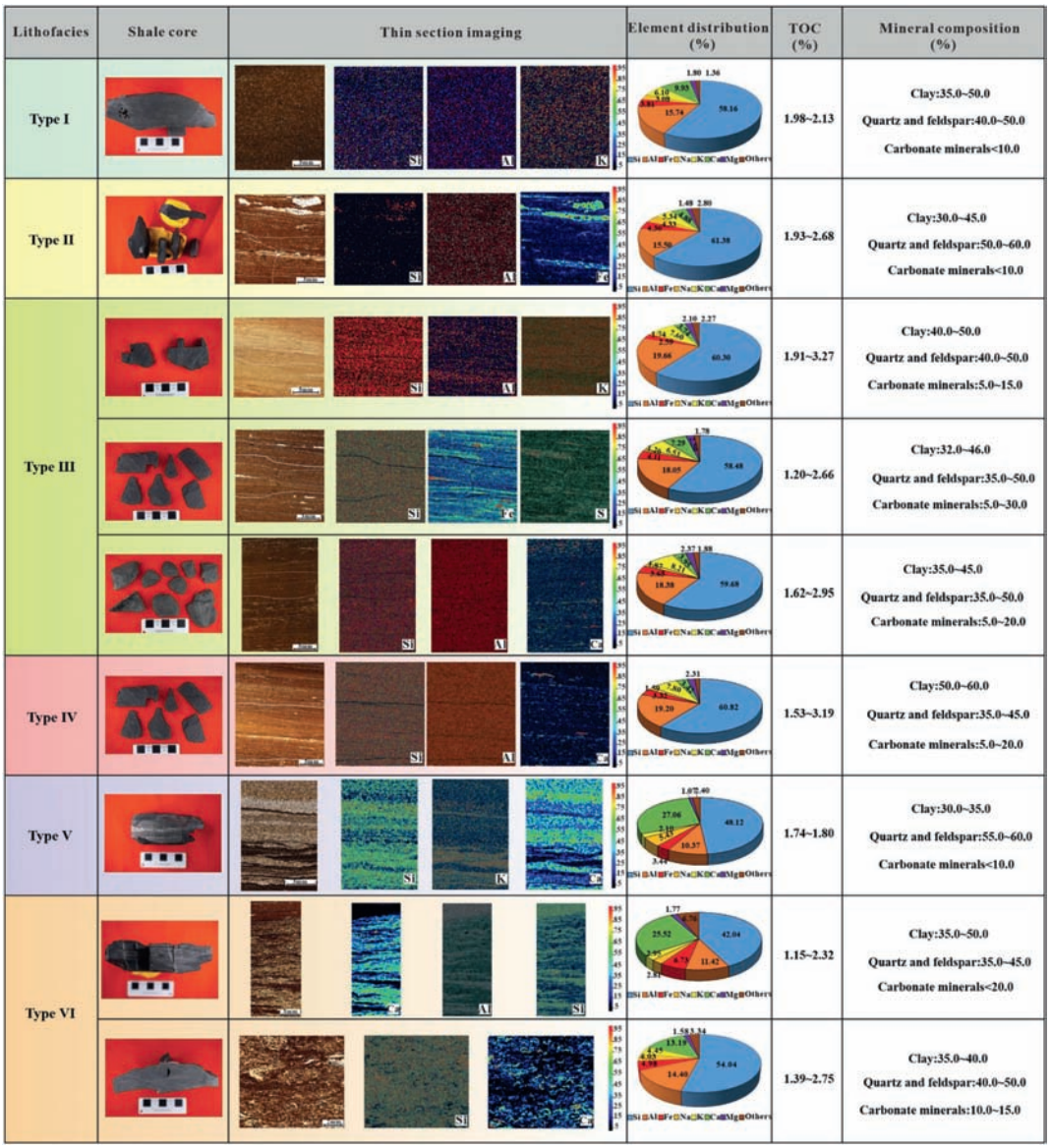


Fig. 6. Shale lithofacies types and characteristics of the K_2qn shale in the Changling Sag.

(58.48%) and Al (18.05%) concentrations, along with significant Ca and K levels. In addition, the III_3 lithofacies is characterized by feldspar grains and biogenic particles distribution. Mineral distributions evolve from isolated to discontinuous and plate-like forms, forming thin laminae of silt and carbonate. The shale has an average TOC of 2.23%, with clay mineral contents ranging from 37.1% to 44.5%, feldspar from 35.8% to 47.5%, and carbonate minerals averaging around 11.1%. The XRF analysis of sample X3-7 reveals Si content of 59.68%, Al at 18.38%, and K at 8.21%.

Type IV lithofacies are dominated by clastic argillaceous layers, with an average TOC of 2.31%. The lithofacies are notable for relatively higher clay mineral content, ranging from 50% to 60%, and feldspar concentrations between 35% and 45%. Sample X1-6 demonstrates typical elemental distributions, with Si at 60.82%, Al at 19.20%, and K at 7.80%.

Compared to previous lithofacies, type V exhibits moderate TOC levels, averaging 1.77%, along with significantly higher feldspar content ranging from 55% to 60%. Clay mineral abundance is relatively lower, between 30% and 35%. These rocks typically display thin laminae of argillaceous, silt, and carbonate assemblages. For example, microscopic examination of sample X2-5 reveals alternating bright and dark laminae, with elemental mapping highlighting differentiated distributions dominated by Si, Ca, and K.

Type VI lithofacies present TOC values ranging from 1.15% to 2.75%, with feldspar and clay minerals showing comparable contents within the range of 30%~50%. These samples are subdivided into combinations of AL and CL or ML. Sample X2-8 exemplifies horizontal superposition of CL and AL, with clear interfaces and undulating sedimentary morphologies. Elemental scanning reveals Si at 42.04%, Ca at 25.52%, and Al at 11.42%. Additionally, sample X2-3 features complex mineralogy with a brownish hue, displaying lighter bands or patches. Detrital grain sizes vary from fine to medium, and compaction or mild metamorphism induces directional alignment of mineral particles. Elemental composition is dominated by Si (54.04%), followed by Al (14.40%) and Ca (13.19%).

3.4. Morphological characteristics of shale pore structures

FE-SEM observations reveal that the K_2qn shale exhibits diverse pore types, including organic matter pores, intraparticle pores, interparticle pores, and micro-fractures (Fig. 7), emphasizing the morphological, dimensional, and spatial heterogeneity of the reservoir. OM pores are sparsely developed, elliptical to subcircular, and typically occur at the nanometer scale (Fig. 7a and b). Localized edge cracking in organic particles is observed, possibly due to shrinkage during hydrocarbon generation (Fig. 7a). OM-clay complexes show irregular or angular pores, with diameters ranging from 10 nm to over 1 μm (Fig. 7c). Intraparticle pores are mainly found within clay aggregates, presenting flocculent structures (Fig. 7d). These aggregates form “card-house” frameworks through edge-to-surface and edge-to-edge contacts. Brittle minerals such as feldspar and dolomite exhibit dissolution induced by organic acid fluids, creating sub-circular to irregular pores with diameters between 0.1 μm and 2 μm (Fig. 7e). These dissolution features often show serrated pore walls, particularly within feldspar grains. Interparticle pores are located at contacts between brittle minerals or between brittle and clay minerals. These pores are typically triangular, polygonal, or elongated voids, heavily influenced by mineralogy, grain alignment, and compaction intensity. Bitumen infilling is occasionally observed, reducing the effective pore space volume (Fig. 7f). Feldspar dissolution followed by the precipitation of euhedral to subhedral crystals further constrains primary porosity (Fig. 7g). Micro-fractures are extensively developed throughout the shale. The formation and extension of these micro-fractures are controlled by variations in the mechanical properties of the minerals, particularly at the interfaces between AL and CL or SL (Fig. 7h). Microfractures are more developed at these interfaces and tend to extend along the laminae boundaries, providing essential migration pathways for shale oil. Additionally, microfractures are sometimes observed around bioclastic grain edges (Fig. 7i). However, the dense packing of shell debris within CL restricts pore connectivity, limiting the available storage space.

3.5. Quantitative characterization of shale pore structures

3.5.1. High-resolution large-area imaging and data analysis

Due to the limited development of SL in the study area, this research focuses on high-resolution imaging and quantitative analysis of CL, ML, AL, and argillaceous layer. The grayscale and mineral distribution images of CL in the sample X2-5, shown in Fig. 8a_1~a_2, reveal a significant accumulation of biological scale particles. Quantitative analysis reveals a surface porosity of 0.90%, with organic pores and microfractures contributing less than 10%, and inorganic fractures account for a notably high contribution of 42.70% (Fig. 8e). SEM observations indicate that the pores are generally absent inside the biological shell, microfractures are present around the shell particles (Fig. 5i). Further analysis of the pore size distribution reveals that inorganic fractures in the range of 500 nm to 1 μm contribute the most to surface area, accounting for 12.25%.

The ML shows a coexistence of various pore types. For samples X2-2 (Fig. 8b_1~b_2) and X2-11 (Fig. 8c_1~c_2), surface porosities are 3.47% and 1.41%, respectively. Like CL characteristics, organic pores and fractures in the ML contribute little to the reservoir space. However, inorganic pores and fractures show significant variation between these samples. In sample X2-2 (Fig. 8f), inorganic pores and fractures contribute 78.59% and 18.93%, respectively, while in sample X2-11, they contribute 71.07% and 27.03% (Fig. 8g). QEMSCAN images reveal a higher concentration of biogenic shell particles in the latter, leading to lower porosity and higher inorganic fracture contribution. Pore size analysis reveals that interparticle pores dominate the space in sample X2-2, contributing 41.87%, with pore sizes primarily above 300 nm. In contrast, the porosity of sample X2-11 is mainly attributed to intraparticle pores and inorganic fractures, with pore sizes ranging from 150 to 500 nm. These differences highlight the mineral composition in the ML leads to significant changes in pore structure and reservoir characteristics.

AL is commonly interbedded with SL or CL, which prompted a detailed study of sample X3-5 to investigate the pore structure characteristics of AL (Fig. 8d_1 and d_2). SEM analysis shows that the porosity of the analyzed AL is 4.17%, with interparticle pores dominating the reservoir space and contributing 41.86% to the porosity (Fig. 8h). Microfractures further enhance the reservoir performance, contributing 26.43%. Observations reveal that the interface between the AL and CL is prone to cracking due to differences in compressive stress, with some microfractures extending to improve pore connectivity and significantly. The contribution of microfractures in the sample X3-5 reaches a peak of 8.25%, mainly concentrated in the 150–300 nm range.

However, as the thickness of the laminae increases, the pore structure of the argillaceous layer structure deteriorates. Taking sample X3-1 as an example (Fig. 9a_1 and a_2), the calculated porosity is 2.22%. It suggests that the shale in the study area is in the middle rock-forming stage, where intense compaction has restricted the development of pore space in the reservoir. Further analysis shows that the contribution of organic pores and organic

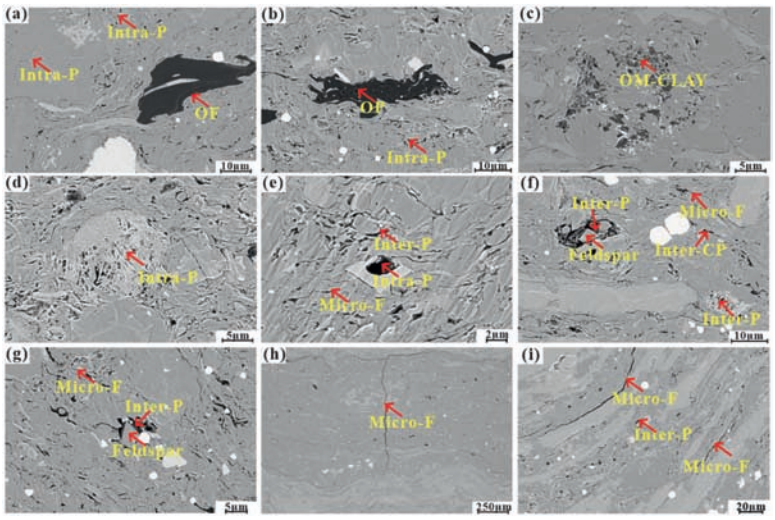


Fig. 7. Pore types and morphological distribution characteristics of K_2qn shale in the Changling Sag. (a) No pores developed within organic matter, with organic fractures observed, sample X2-1; (b) Some pores developed in the organic matter, sample X2-5; (c) Intraparticle pores developed within organic matter-clay mineral composite, sample X3-5; (d) Intraparticle pores developed within clay aggregates, sample X2-2; (e) Dolomite grains exhibit dissolution pores with diameters up to 2 μm, sample X2-1; (f) Bitumen and subhedral feldspar filling interparticle pores, sample X2-11; (g) Anhedral feldspar grains filling pores, sample X2-5; (h) Microfractures developed at the interface between AL and CL, extending further and vertically penetrating AL, sample X2-6; (i) Bioclastic grains within CL surrounded by microfractures, sample X2-6. Intra-P: intraparticle pore; OF: organic matter pore; OM: organic matter; Inter-P: interparticle pore; Micro-F: microfracture.

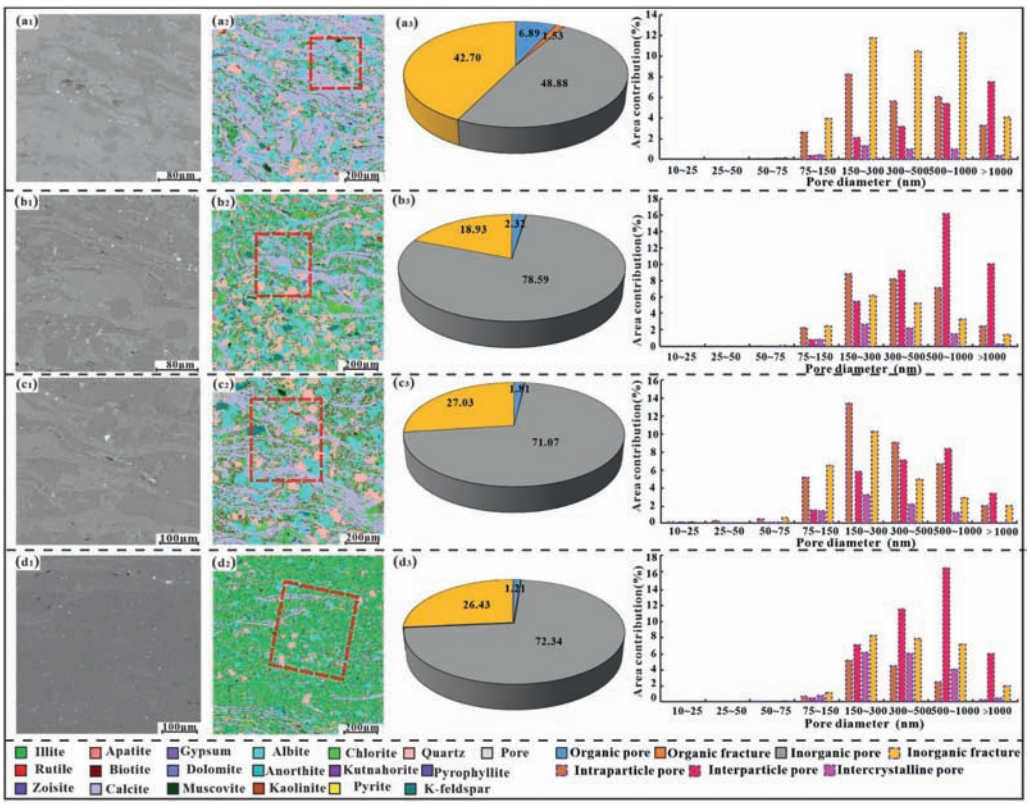


Fig. 8. Integrated MAPS and QEMSCAN results illustrating laminae characteristics of the K_2qn shale. Red boxes in the mineral distribution maps indicate the areas corresponding to the grayscale images. (a_1~a_3) CL images of sample X2-5; (b_1~b_3) ML images in sample X2-2; (c_1~c_3) ML images in sample X2-11; (d_1~d_3) AL images in sample X3-5.AL: argillaceous laminae; CL: carbonate laminae; ML: mixed laminae.

fractures is less than 5.00%, while the contributions of inorganic pores and inorganic fractures range from 60.00% to 85.00% and 10.00%–35.00%, respectively (Fig. 9a_3). Pore size distribution indicates that the most significant pore contribution is in the 150 nm to 1 μm range, mainly consisting of intraparticle pores, interparticle pores, and inorganic fractures. Furthermore, the pore structure has been improved for the disturbed argillaceous layer (Fig. 9b_1~c_2). The porosity of the sample X2-1 is 3.28%, with inorganic pores contributing 60.00%–65.00%, and inorganic fracture areas contributing 30.00%–40.00% (Fig. 9b_3). Interparticle

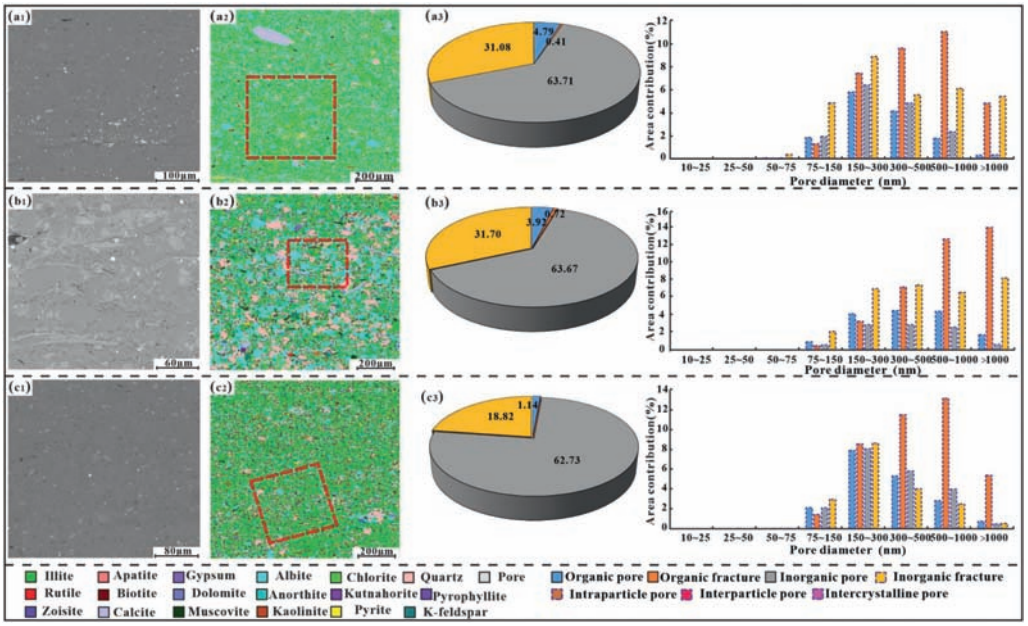


Fig. 9. Integrated MAPS and QEMSCAN results illustrating argillaceous layer characteristics of the K_2qn shale. Red boxes in the mineral distribution maps indicate the areas corresponding to the grayscale images. (a_1~a_3) Homogeneous argillaceous layer the sample X3-1; (b_1~b_3) Disturbed argillaceous layer within the sample X2-1; (c_1~c_3) Clastic-bearing argillaceous layer within sample X3-7.

pores in this sedimentary structure are well developed, especially above 300 nm, contributing 30.00%–35.00% of the reservoir space. The QEMSCAN image shows an increased feldspar content with larger particle sizes, alleviating pore space compression and preserving pores associated with clay minerals. Micrometer-sized microfractures in the sample X2-1 contribute 8.32%. Similarly, the pore structure of the argillaceous layer containing debris is also well developed, as seen in the sample X3-7, with a surface porosity of 3.40% and interparticle pores predominantly in the 300 nm to 1 μm range (Fig. 9c_3).

3.5.2. LTNA analysis

The nitrogen adsorption-desorption isotherms of K_2qn shale are predominantly Type IV with anti-S characteristics, indicating a complex pore structure and wide pore size distribution (Fig. 10a–c). There are pronounced hysteresis loops predominantly of type H2 and H3 in the shale (Sing, 1985; Thommes et al., 2015). The former suggests the presence of flared or bottleneck-shaped pores, with narrow throats and wide bodies. The latter is associated with fracture- or plate-like pores, showing unsaturated adsorption behavior and a gentle desorption slope. Pore size and volume distribution curves exhibit multi-modal features, with significant peaks in the 1–2 nm, 2–5 nm, and 30–60 nm ranges, highlighting well-developed micropores and mesopores (Fig. 10d ~ f). The considerable pore volumes are observed in samples from Well X1, ranging from 1.85 to 3.74 cm^3/100 g, with an average of 2.64 cm^3/100 g. Samples from Well X2 show the pore volumes from 1.00 to 2.43 cm^3/100 g, averaging 1.80 cm^3/100 g. Samples from Well X3 have the lowest pore volumes, ranging from 0.85 to 1.80 cm^3/100 g, with an average of 1.21 cm^3/100 g. These results reflect significant heterogeneity in reservoir space development within the K2qn shale reservoir.

3.5.3. MICP analysis

The mercury intrusion curve of the K_2qn shale shows three distinct stages (Fig. 11a–c). First, slow mercury intake occurs at low pressure, corresponding to the initial filling of micrometer-scale macropores. Then, gradual intrusion at medium pressure indicates restricted pore throat connectivity. Finally, a sharp increase at high pressure reflects a broad pore size distribution. Notably, mercury intake continues to rise even at the maximum pressure, likely due to the expansion of mercury volume under high-pressure conditions (Sun et al., 2020). The mercury withdrawal curve lags behind the intrusion curve, showing pronounced hysteresis with a gentle slope and removal efficiencies below 50%, which further indicates limited pore connectivity in the shale. Pore size distribution reveals that the majority of pores are smaller than 100 nm, with a unimodal feature (Fig. 11d ~ f). The pore volume is mainly provided by pores smaller than 10 nm range, emphasizing the importance of nanoscale pores as the primary reservoir space. Moreover, pores larger than 10 μm are not considered to exclude anomalous data from sample preparation. Significant heterogeneity is observed in the cumulative mercury intrusion volumes across shale samples. Samples from Well X1 show the highest pore development, with volumes ranging from 0.62 to 1.53 cm^3/100 g and an average of 1.09 cm^3/100 g. In comparison, samples from Well X2 exhibit moderate pore volumes, between 0.38 and 1.33 cm^3/100 g, with an average of 0.87 cm^3/100 g. Samples from Well X3 have the lowest pore volumes, ranging from 0.17 to 0.57 cm^3/100 g, averaging 0.45 cm^3/100 g. Notably, some samples contain pores larger than 10 μm, indicating favorable compressibility and potential for hydraulic fracturing.

3.6. Evaluation of shale oil distributions

Samples from wells X1 and X3 are collected using a pressure-holding and sealed coring technique, effectively minimizing light hydrocarbon volatilization. In contrast, long-term storage led to partial light hydrocarbon loss in samples from Well X2 (Xie et al., 2019), necessitating correction of their S_1 values using test data from the adjacent Well JY 1HF (Xu et al., 2021). The oil saturation index (OSI), defined as the ratio of S_1 to total organic carbon, serves as a critical parameter for assessing the potential presence of movable hydrocarbons in shale oil reservoirs, which is conventionally obtained from standard Rock–Eval pyrolysis measurements. The OSI suggests higher shale oil mobility in samples from

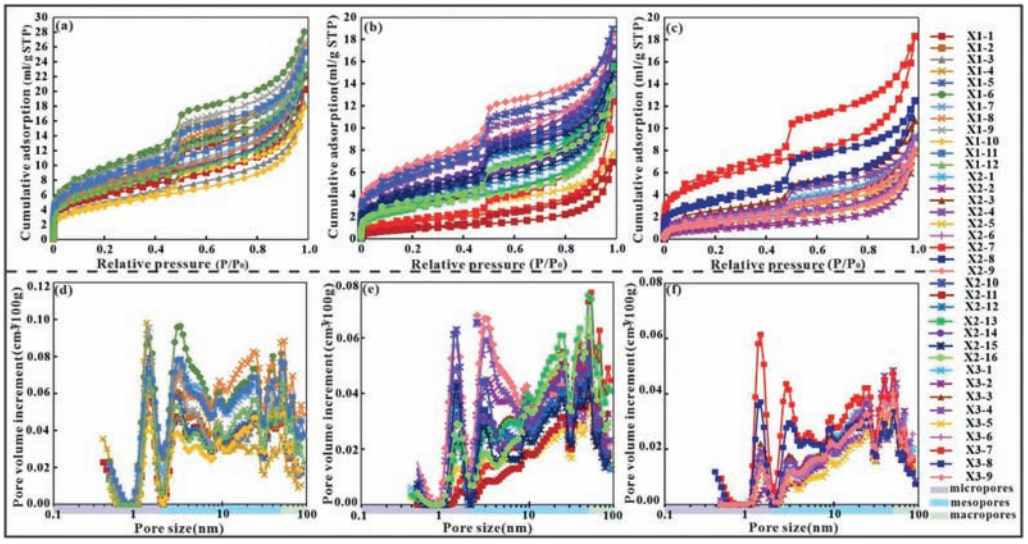


Fig. 10. Nitrogen adsorption-desorption isotherms and corresponding pore size distribution characteristics of the K_2qn shale. (a, d) Well X1; (b, e) Well X2; (c, f) Well X3.

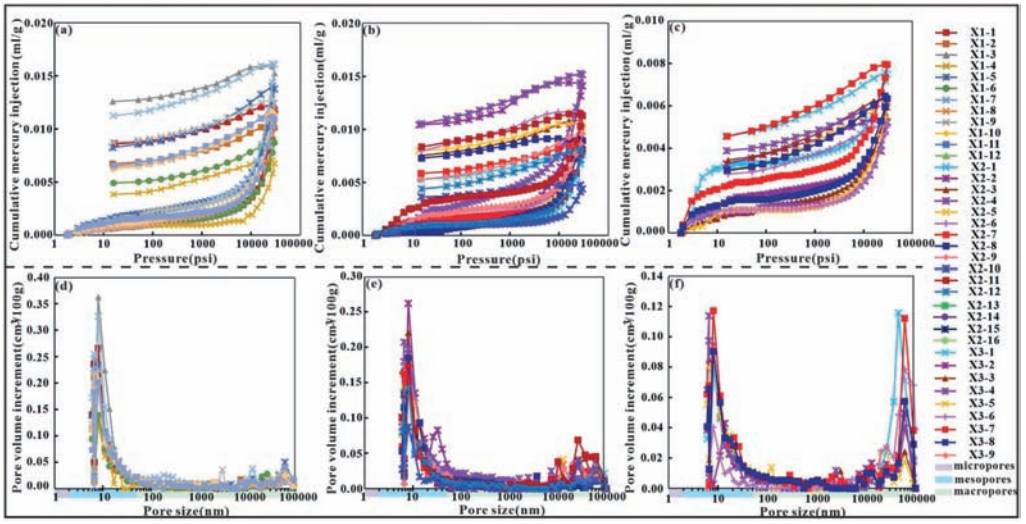


Fig. 11. Mercury intake-mercury withdrawal curves and corresponding pore size distribution characteristics of the K_2qn shale. (a, d) Well X1; (b, e) Well X2; (c, f) Well X3.

wells X1 (80.04–224.92 mg/g) and X2 (51.07–312.08 mg/g). In comparison, samples from well X3 exhibit lower OSI values, ranging from 38.08 to 122.13 mg/g, indicating poorer mobility and reduced resource utilization potential. By integrating OSI and production index (PI) data (Fig. 12a), it is evident that most samples from wells X1 and X2 fall within the shale oil enrichment zone, whereas those from Well X3 generally lie outside this zone. The PI-Tmax plot further indicates that shale oil in Well X1 results from both in-situ organic matter pyrolysis and exogenous hydrocarbon charging, whereas shale oil in wells X2 and X3 primarily originates from local pyrolysis within a source-reservoir integrated system (Fig. 12b).

To further quantify hydrocarbon migration behavior, this study employs the ΔQ parameter calculation method proposed by Hu et al. (2018), which is grounded in the principle of mass conservation. The micro-migration hydrocarbon quantity (ΔQ) quantifies the difference between the original hydrocarbon generation potential and the present pyrolysis-derived potential. A positive ΔQ value denotes that hydrocarbons have been expelled after the threshold for in-situ retention was met, whereas a negative ΔQ value reflects insufficient indigenous hydrocarbon generation and suggests that the system is dominated by externally sourced hydrocarbons. By integrating the measured S_1 values with hydrocarbon generation yields, the hydrocarbon migration characteristics of the K_2qn shale are presented as follow.

$$HI = HI_0\left\{1 - \exp\left[-\left(\frac{T_{max}}{\beta}\right)^{\theta}\right]\right\} \tag{1}$$

$$T_R = \frac{HI_0 - HI}{HI_0} \tag{2}$$

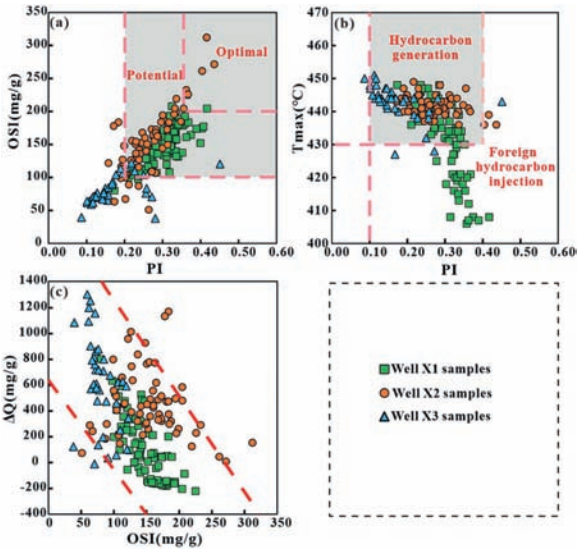


Fig. 12. Interpreted oil content characteristics of the K_2qn shale. (a) Cross-plot of production index (PI) versus oil saturation index (OSI); (b) cross-plot of PI versus Tmax; (c) cross-plot of OSI parameter and ΔQ variation.

$$HI_s = \frac{HI}{1 - T_R} \tag{3}$$

$$\Delta Q = HI_s - I_{HGP} \tag{4}$$

$$I_{HGP} = \frac{S_1 + S_2}{TOC} \times 100 \tag{5}$$

where the HI and Tmax values are derived from rock-eval pyrolysis analyses; HI_0 represents the original hydrogen index prior to thermal alteration; TR denotes the transformation ratio corresponding to the peak pyrolysis temperature; parameters β and θ are fitting coefficients obtained through nonlinear regression of extensive pyrolysis datasets across various kerogen types (Hu et al., 2021).

The results reveal a significant negative correlation between ΔQ and OSI (Fig. 12c), suggesting that exogenous hydrocarbon injection not only increases oil content but also enhances the saturation and mobility of shale oil. Conversely, hydrocarbon expulsion reduces oil enrichment and lowers OSI values. Samples from Well X1 show ΔQ values ranging from −220.22 mg/g to 801.91 mg/g, with approximately 40% exhibiting negative values. This indicates that these samples possess favorable storage capacity and connectivity. In contrast, ΔQ values from wells X2 and X3 mostly fall within the range of 0~1300 mg/g, reflecting a dominantly self-sourced enrichment system and weak migration or charging effects. These findings align with oil-source diagnostics inferred from the PI-Tmax plot (Fig. 12b). Shale oil characteristics are further assessed using quantitative fluorescence parameters. The fluorescence spectra of all samples display single-peaked, left-skewed distributions with λ_{max} around 380 nm, indicating compositionally uniform shale oil of medium to heavy type. R_1 values range from 1.8 to 5.4, with values generally exceeding 3.0 in wells X2 and X3, whereas samples from Well X1 exhibit lower values, suggesting higher maturity oil in the reservoir. The average normalized fluorescence intensities of QGF-E and TSF for samples from wells X1, X2, and X3 are 15509.0/35186.8 pc, 12482.7/21496.3 pc, and 16102.0/36336.6 pc, respectively (Table 2).

4. Discussions

4.1. Shale reservoir properties differences

Given the disparate pore size ranges addressed by various experimental methodologies, a singular analytical approach is inadequate for comprehensively characterizing the microscopic pore distribution characteristics of shale reservoirs (Rexer et al., 2014). In this study, the pore diameter of 50 nm is chosen as the threshold for integrating data derived from fluid injection methods. Based on the integrated dataset, the total pore volume of the K_2qn shale ranges from 0.74 to 3.55 cm^3/100 g, with a mean value of 1.82 cm^3/100 g. According to pore size classification criteria (Brunauer et al., 1940), the pores are subdivided into macropores (>50 nm), mesopores (2–50 nm), and micropores (<2 nm). The analytical results underscore that mesopores are the predominant contributors to the pore system in the shale, comprising between 68.34% and 93.58% of the total pore volume. Micropores also represent a significant fraction, with volume contributions ranging from 2.45% to 24.43%. Besides, macropores occupy a relatively minor proportion of the pore volume, contributing between 1.82% and 16.38%. From the perspective of the distribution characteristics, the samples from Well X1 exhibit the highest storage capacity, with total pore volumes spanning from 1.81 to 3.55 cm^3/100 g, and an average of 2.52 cm^3/100 g. In addition, shale samples from Well X2 demonstrate moderate storage properties, with total pore volumes ranging from 0.81 to 2.29 cm^3/100 g and a mean of 1.62 cm^3/100 g. Conversely, samples from Well X3 show the lowest storage capacity, with total pore volumes between 0.70 and 1.70 cm^3/100 g, yielding a mean value of 1.07 cm^3/100 g.

Significant differences in pore types, pore size distributions, and reservoir characteristics are observed across these K_2qn shale lithofacies (Fig. 13). Type I lithofacies shale is characterized by downward-trending nitrogen adsorption and capillary pressure curves, indicative of dominant ink-bottle-shaped pores and a relatively narrow hysteresis loop. The pore size distribution is predominantly unimodal, with a peak between 30 nm and 40 nm (Fig. 13a). As a result, the average total pore volume is relatively low, ranging from 1.01 cm^3/100 g, suggesting limited reservoir space and weak seepage capacity. Type II lithofacies are characterized by intermediate nitrogen adsorption capacity and mercury intrusion volumes. The hysteresis loop is relatively small, and the pore system is dominated by mesopores with a simpler distribution pattern. The total pore volumes range from 1.12 to 2.63 cm^3/100 g, indicating more abundant pore space compared to Type I (Fig. 13b). In type III lithofacies, nitrogen adsorption capacity increases significantly. Specifically, shale of III1 lithofacies predominantly develops ink-bottle-shaped pores, with an average total pore volume of 1.25 cm^3/100 g (Fig. 13c). Types III2 and III3 exhibit stronger reservoir capacities, with total pore volumes ranging from 1.81 to 3.10 cm^3/100 g and 1.70–3.31 cm^3/100 g, respectively (Fig. 13d and e). Compared to types I and II, type III lithofacies preserve reservoir space more effectively and exhibit better permeability under external disturbances or the incorporation of clastic particles. Type IV shale lithofacies exhibit comparable reservoir capacities to type III, with total pore volumes ranging from 1.00 to 3.55 cm^3/100 g and an average of 2.05 cm^3/100 g (Fig. 13f). However, the reservoir quality in this lithofacies is strongly influenced by detrital particle content. As the abundance of detrital particles increases, the total pore volume tends to decrease. Additionally, micropores comprise a relatively large proportion in type IV shale, highlighting the significant contribution of clay mineral-associated pores to the overall reservoir space. Type V shale lithofacies

Table 2
The distribution of oil content parameter values of the K_2qn shale.

Well	Sample No.	ΔQ (mg/g)	QGF-E Intensity (pc)	TSF Intensity (pc)	R_1	R_2
X1	X1-1	338.82	30583.56	68219.63	2.80	3.94
	X1-2	93.89	45400.48	102811.21	2.66	3.80
	X1-3	232.20	11852.31	27362.75	2.72	3.86
	X1-4	156.27	8023.41	18264.06	2.38	3.55
	X1-5	626.11	15501.59	35899.02	2.23	3.16
	X1-6	35.51	15113.47	34331.01	2.20	3.13
	X1-7	−166.37	12356.31	28006.95	2.22	3.14
	X1-8	161.27	17706.91	40455.18	2.22	3.14
	X1-9	−43.00	18791.93	42448.33	2.25	3.18
	X1-10	−161.44	9451.51	21235.19	2.15	3.01
	X1-11	−33.21	16356.69	37666.98	2.20	3.03
	X1-12	61.34	20055.22	45926.23	2.12	2.95
X2	X2-1	558.60	16998.36	30206.19	5.28	8.40
	X2-2	320.10	17211.33	29912.16	5.10	7.93
	X2-3	426.86	15383.84	26453.59	5.37	8.16
	X2-4	459.67	7730.87	12937.04	4.24	6.90
	X2-5	746.09	10175.33	17533.18	5.01	7.90
	X2-6	1133.92	8083.04	13778.99	4.11	6.72
	X2-7	766.44	24688.15	42213.38	4.82	7.56
	X2-8	442.24	16906.71	28901.52	4.99	7.81
	X2-9	308.91	9688.73	16474.03	4.17	6.74
	X2-10	451.62	12437.75	21111.35	4.73	7.67
	X2-11	838.40	16691.42	28333.05	4.27	7.00
	X2-12	45.93	10194.35	17374.87	3.89	6.20
	X2-13	516.03	17337.89	29775.73	4.55	7.74
	X2-14	474.43	10558.74	18421.68	4.21	7.00
	X2-15	480.62	11566.38	19818.06	4.33	6.97
	X2-16	585.56	25621.60	44534.57	4.69	7.52
X3	X3-1	675.81	24789.62	55984.52	3.57	5.05
	X3-2	477.98	21602.96	49079.22	4.07	5.59
	X3-3	474.52	14954.97	33508.27	3.47	4.92
	X3-4	1254.54	12953.20	29754.72	3.18	4.62
	X3-5	1157.57	13894.75	31363.49	3.22	4.69
	X3-6	760.79	21794.88	49449.66	3.83	5.42
	X3-7	593.42	19228.02	43855.89	3.47	4.86
	X3-8	197.57	6337.05	14257.08	2.99	4.11
	X3-9	793.90	16981.39	37845.38	3.40	4.81

display the least developed pore systems, with a total pore volume of only 0.99 cm^3/100 g (Fig. 13g). Thin-section analysis reveals that the AL are relatively thin, with well-developed carbonate components, which collectively constrain pore development and limit the overall storage capacity. Conversely, interbedded assemblages dominated by AL demonstrate better pore development, with total pore volumes reaching 1.84 cm^3/100 g. Type VI shale lithofacies exhibit relatively large hysteresis loop areas, and their reservoir performance is notably influenced by detrital particle content. An increase in detrital particles corresponds to a decline in overall reservoir capacity. Specifically, shale with interbedded sedimentary structures displays total pore volumes ranging from 0.74 to 2.24 cm^3/100 g (Fig. 13h), and those with mixed laminae range from 0.81 to 1.98 cm^3/100 g (Fig. 13i). In summary, comparative analysis reveals that type III, V, and VI shale lithofacies demonstrate the most favorable reservoir capacities.

4.2. Controlling factors of shale pore structures

4.2.1. TOC and mineral composition

No consistent correlation is observed between total organic carbon content and pore volumes in the K_2qn shale, in contrast to findings from highly mature marine shale systems. This discrepancy is primarily attributed to the relatively low thermal maturity of the K_2qn shale, which remains largely within the oil generation window. Under these conditions, organic matter has undergone limited thermal cracking, restricting the formation of primary organic pores. Notably, the relationship between TOC and pore volume varies significantly among wells. In Well X1, a weak positive correlation is observed, particularly with macropore volume (Fig. 14a_1~a_4), suggesting relatively higher organic matter content and a more advanced stage within the oil generation window. During diagenesis, acidic fluids generated from organic matter pyrolysis likely interacted with inorganic minerals, promoting pore restructuring and the formation of secondary pores. In contrast, samples from Wells X2 and X3 exhibit a negative correlation between TOC and pore volumes (Fig. 15a_1~a_3). These wells are located in semi-deep to marginal lacustrine depositional settings, where shale maturity is lower. A significant portion of the organic matter remains thermally immature and exists predominantly as bitumen within pore spaces, reducing effective porosity.

Based on 30 representative K_2qn shale samples, the influence of clay minerals and brittle minerals on full-scale pore volume was systematically assessed. Overall, neither clay minerals nor quartz–feldspar-rich brittle minerals exhibit a consistent correlation with total pore volume across all samples. Similar to TOC, the effect of mineral composition on pore development is well controlled by well-specific conditions. In Well X1, clay mineral content (Vsh) shows a positive correlation with pore volume (Fig. 14b_1~b_4), largely due to the predominance of illite and illite-smectite mixed-layer minerals (Hart et al., 2023). During the thermal evolution of smectite, dehydration leads to structural reorganization and lattice collapse, generating abundant nanoscale pores and microfractures (Chang et al., 2022). Additionally, the release of interlayer water under confined compaction conditions may induce excess pore pressure, helping preserve pore integrity and mitigate structural densification. Conversely,

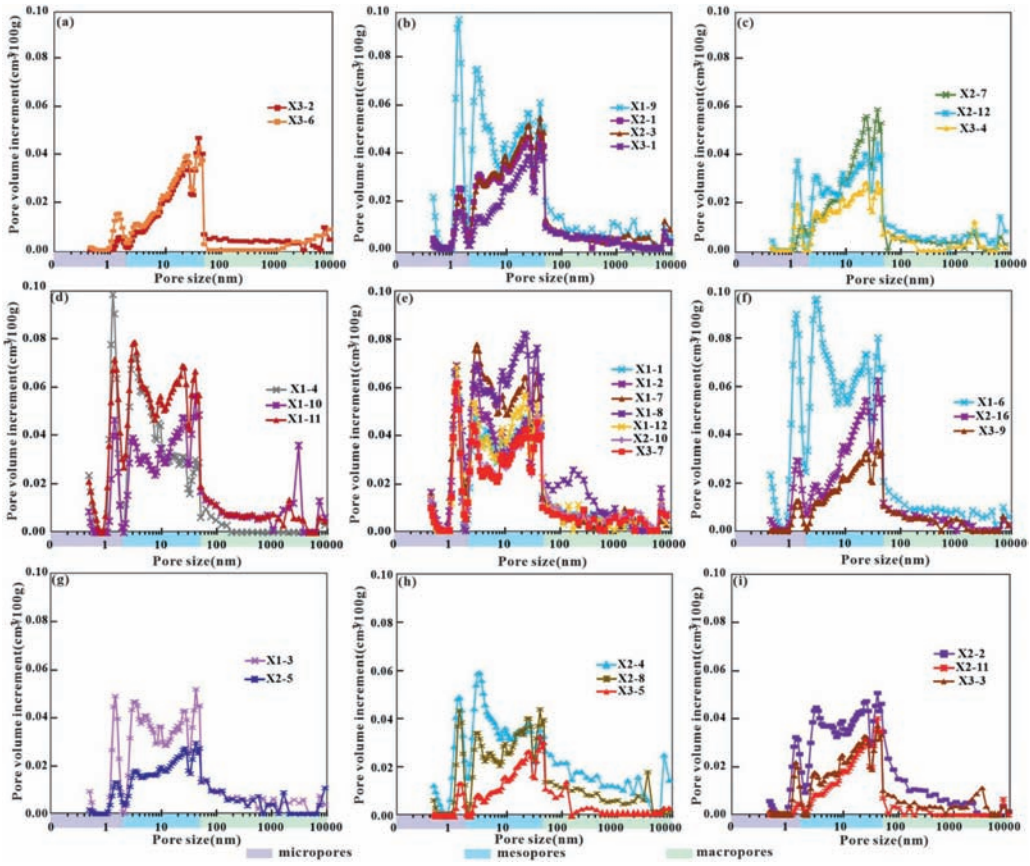


Fig. 13. Full-scale pore size distribution characteristics of K_2qn shale across different lithofacies.

feldspar and quartz contents (Vsi) in Well X1 display a negative correlation with total pore volume, particularly for micropores (Fig. 14c_1~c_4), suggesting that enrichment in brittle minerals can inhibit effective pore development. Diagenetic dissolution of feldspar and quartz by organic acids may form secondary pores and enhance porosity (He et al., 2022a, b), the efficiency of this process is strongly dependent on organic matter abundance, acid concentration, and the presence of fluid pathways (Chen et al., 2017).

In Wells X2 and X3, no significant correlation is observed between clay content and total pore volume, likely due to widespread bitumen occlusion in low-maturity shale matrices. The formation of organic–mineral composite structures may further reduce pore connectivity. To better quantify clay mineral influence, a composite index defined as the clay-to-TOC ratio was introduced (Fig. 15b_1~b_4). This index shows a positive correlation with total pore volume in Well X2 (coefficients 0.33–0.66) and with macropore volume in Well X3 (coefficient 0.46), indicating that under low thermal maturity, clay minerals exert a more pronounced effect in shales with relatively low organic matter content. Similarly, a feldspar-TOC composite index was evaluated to assess the coupled effect of feldspar and organic matter. In Wells X2 and X3, this index exhibits a significant negative correlation with pore volume (Fig. 15c_1~c_4), suggesting that feldspar enrichment, combined with low organic maturity, inhibits pore network development. Quartz, derived from both terrigenous clastic input and authigenic growth, frequently crystallizes within pores, limiting storage capacity (Bai et al., 2022). Although feldspar can theoretically form secondary dissolution pores, low thermal evolution constrains this process, and closed diagenetic conditions promote authigenic mineral precipitation that occludes pore space. SEM observations confirm widespread interparticle pore filling by authigenic minerals (Fig. 7), substantially reducing pore connectivity and overall reservoir quality. Carbonate minerals show only weak correlations with pore volume, indicating minimal influence on pore development in the studied samples.

4.2.2. Sedimentary structure

Shale with distinct sedimentary architectures exhibit pronounced variations in pore development and reservoir performance. Quantitative analyses reveal that massive structural shales generally have low nitrogen adsorption capacity and limited cumulative mercury intrusion, reflecting restricted storage space and poor connectivity. In contrast, shales with layered or laminated architectures display more developed pore systems and improved reservoir quality.Among these, carbonate laminae typically form dense, tightly packed microstructures where pore space is primarily controlled by microfractures, resulting in the lowest porosity and limited reservoir effectiveness. For example, sample X2-11 exhibits relatively low pore volume due to high biological detritus content.When argillaceous laminae are interbedded with rigid layers, microfracture penetration enhances pore connectivity, expanding effective reservoir space and partially mitigating compaction-related pore loss. Even thick, homogeneous argillaceous layers, which typically exhibit low porosity, may develop improved pore networks through localized biological disturbances or clastic inputs. Such processes remodel interparticle pores and induce inorganic fracturing, enhancing overall pore structure and reservoir performance. These observations highlight the critical role of sedimentary architecture in controlling pore heterogeneity and emphasize the interplay between depositional

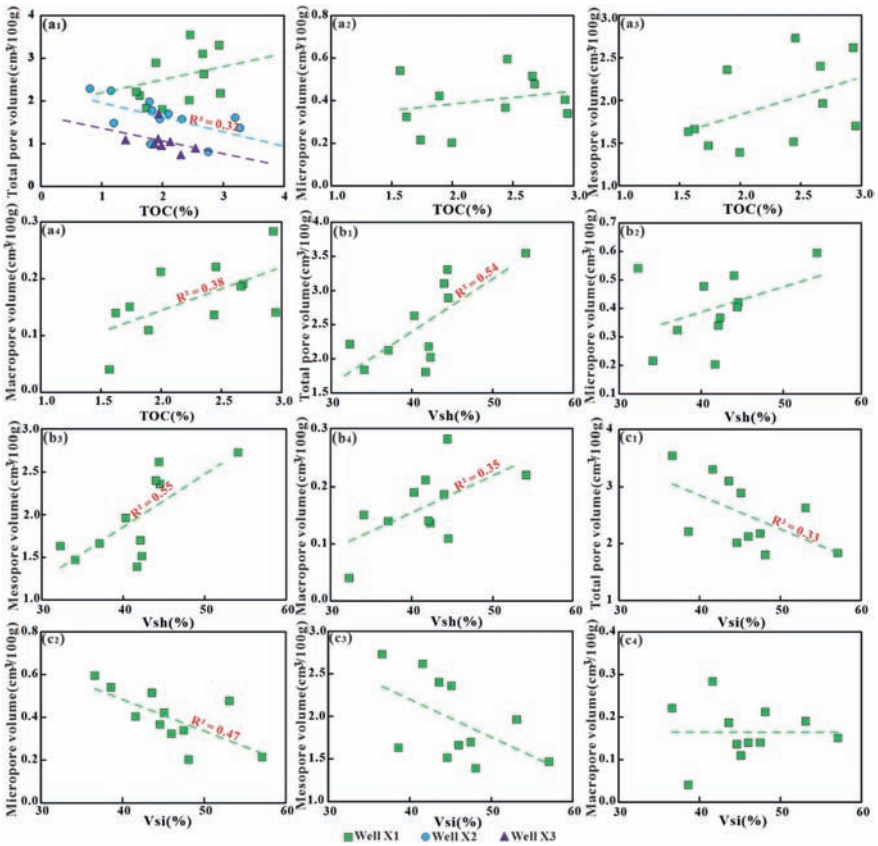


Fig. 14. Correlation analysis of TOC, mineral composition, and pore volume in the K_2qn shale of Well X1 (A correlation coefficient of less than 0.3 is considered to a negligible correlation). Vsh: clay mineral contents; Vsi: feldspar and quartz contents.

features and diagenetic modifications in shaping shale reservoir quality.

4.3. Shale oil accumulation models establishment

Lithofacies, as a comprehensive geological entity encompassing sedimentary environment, organic matter distribution, mineralogical composition, and pore characteristics, plays a decisive role in shale oil enrichment potential. Therefore, understanding the hydrocarbon generation and storage characteristics of different lithofacies is essential for advancing the comprehension of shale oil accumulation mechanisms and provides a scientific foundation for identifying favorable target intervals. Type I lithofacies is characterized by medium to high organic matter content. However, its compact pore structure limits reservoir performance. The generally high ΔQ values indicate that a substantial portion of the generated hydrocarbons has been expelled during thermal maturation, resulting in a typical "high generation-low accumulation" pattern. Consequently, the lithofacies demonstrates low hydrocarbon enrichment potential and is not regarded as a favorable target for shale oil exploration. In addition, type II shale lithofacies is primarily composed of argillaceous layers, with medium organic matter content and certain advantages in pore structure. For example, sample X1-9 has developed a relatively well-formed pore network, demonstrating some capacity for hydrocarbon resource accumulation. Negative ΔQ values observed in some samples indicate external hydrocarbon charging. Type III lithofacies is considered the most prospective in the study area, exhibiting high organic matter content and strong hydrocarbon generation potential. Although III1 shale lithofacies generally exhibit high oil content, their limited pore volume and strong expulsion capacity result in low movable oil content. However, under tectonic disturbance or clastic-rich depositional conditions, interparticle pores and inorganic fractures are better developed in the III2 and III3 shale lithofacies, forming more effective storage spaces and fluid migration pathways. Moreover, type IV lithofacies is dominated by high clay mineral content, which results in a more compact pore system and limited reservoir performance. The elevated ΔQ values suggest that the shale mainly facilitates hydrocarbon expulsion. Additionally, the high clay content presents technical challenges for hydraulic fracturing and post-development operations. Furthermore, types V and VI lithofacies, predominantly found in wells X2 and X3, are typically well-laminated with medium to high organic matter content. Their pore systems are dominated by macropores and interconnected microfractures, providing effective storage space and facilitating hydrocarbon migration. Interbedded laminae often host microfractures that enhance pore connectivity. Consequently, these lithofacies in wells X2 and X3 represent favorable targets, exhibiting higher overall oil-bearing capacity and enhanced hydrocarbon enrichment potential.

In well X1, type III shale lithofacies are predominant, with shale oil enrichment primarily influenced by the migration of hydrocarbons, exemplifying a typical migration-accumulation system (Fig. 16a). In addition, wells X2 and X3 are predominantly characterized by laminated shale of types V and VI, where hydrocarbon accumulation is largely driven by the in situ thermal conversion of indigenous organic matter, reflecting a self-sourced accumulation model (Fig. 16b and c). This contrast not

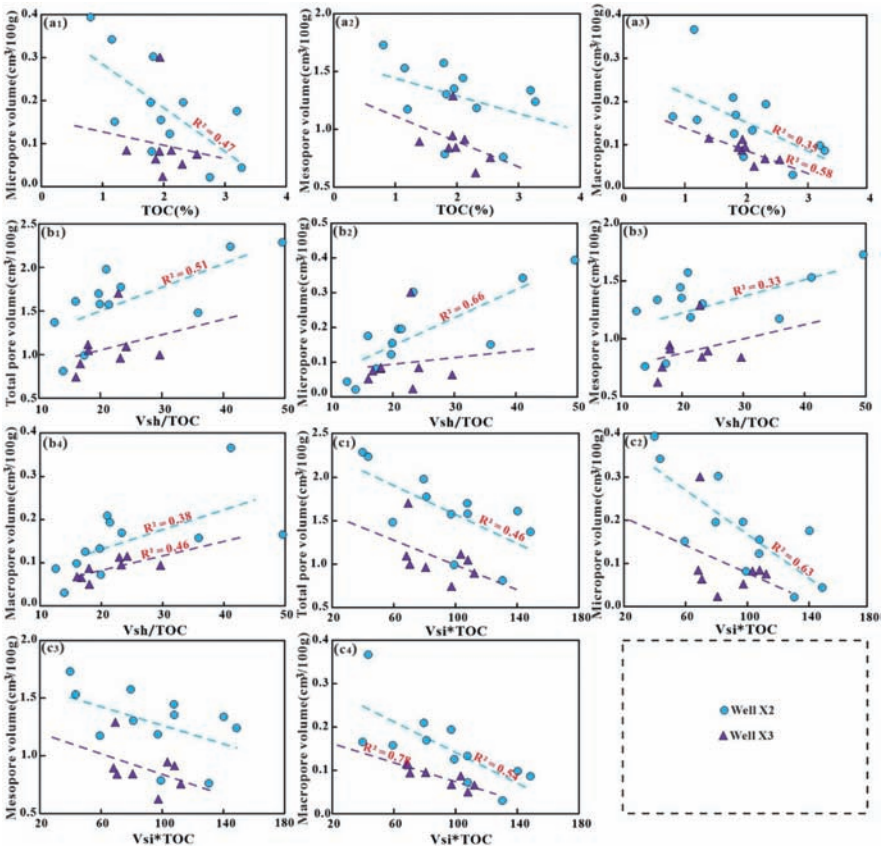


Fig. 15. Correlation analysis of TOC, mineral composition, and pore volume in the K_2qn shale of wells X2 and X3 (A correlation coefficient of less than 0.3 is considered to a negligible correlation). Vsh: clay mineral contents; Vsi: feldspar and quartz contents.

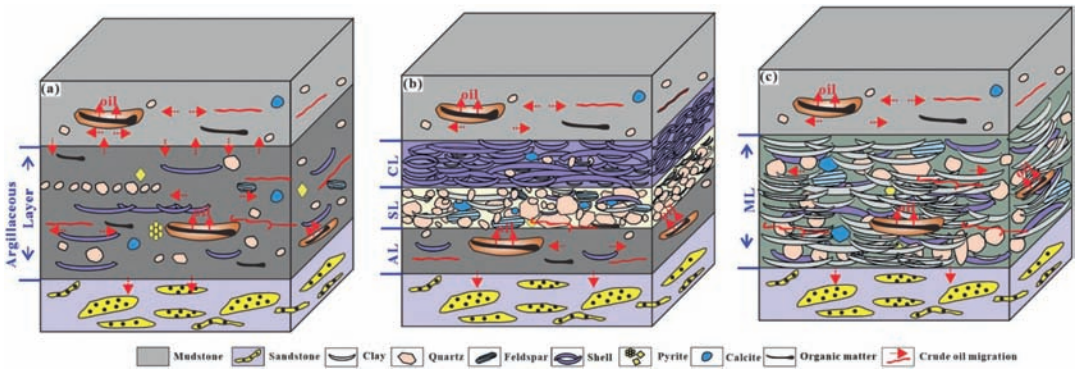


Fig. 16. Shale oil enrichment model for the K_2qn shale. (a) Migration-dominated accumulation in layered mixed shale with medium to high organic matter; (b) in situ accumulation in laminated siliceous shale with moderate organic matter; (c) in situ accumulation in laminated mixed shale with medium to high organic matter. AL: argillaceous laminae; CL: carbonate laminae; ML: mixed laminae; SL: silt laminae.

only underscores the diversity of shale oil enrichment mechanisms but also provides theoretical insights and practical guidance for the exploration and development of different shale lithofacies.

5. Conclusions

This study focuses on the shale intervals of the lower Qingshankou Formation, integrating a comprehensive suite of multi-scale analytical techniques to investigate lithofacies classification, reservoir space characteristics, and hydrocarbon-bearing potential. The following key conclusions were drawn:

(1) The K_2qn shale is characterized by high organic matter abundance, strong hydrocarbon generation potential, and elevated clay mineral content. Based on TOC, mineralogical composition, and sedimentary structures, six lithofacies types are identified. Reservoir space is primarily composed of interparticle pores and microfractures, with type III (layered mixed shale with medium–high TOC), type V (laminated siliceous shale with medium TOC), and type VI (laminated mixed shale with medium–high TOC) exhibiting superior pore connectivity and storage capacity. (2) Pore structure evolution is jointly controlled by organic matter content, mineralogy, lamination development, and

diagenetic processes. Clay minerals contribute positively to nanopore development, while feldspar can reduce porosity through authigenic mineral precipitation. At early thermal maturity stages, the mineralogical influence on pore morphology is further amplified by organic matter transformation. Moreover, compacted carbonate laminae and homogeneous argillaceous layer are associated with low porosity and poor reservoir quality. In contrast, disturbed and detrital-rich argillaceous layer exhibit improved pore development due to enhanced resistance to compaction and the presence of microfractures.

(3) Type III presents the most favorable reservoir space, where shale oil enrichment is predominantly driven by exogenous hydrocarbon injection, representing a typical migration-accumulated system with relatively light oil fractions. In contrast, shale oil accumulation in types V and VI is primarily controlled by in-situ organic matter transformation and residual hydrocarbon retention, forming a self-sourced, self-reservoired in-situ accumulation system.

CRediT authorship contribution statement

Jialin Wan: Writing – original draft, Formal analysis, Data curation, Conceptualization. **Lang Liu:** Funding acquisition. **Qifeng Jia:** Investigation. **Mengmeng Liu:** Investigation. **Zhiyu Fang:** Investigation.

Funding

This research was financially supported by National Science Fund for Excellent Young Scholars (52222404).

Declaration of competing interest

The authors declare no competing financial interest.

Acknowledgments

I would like to express my sincere gratitude to Jilin Oilfield and the Research Institute of Petroleum Exploration and Development, China National Petroleum Corporation, for generously providing the samples essential to this study.

References

Bai, B., Dai, C., Hou, X., Liu, X., Wang, R., Yang, L., Li, S., He, J., Dong, R., 2022. Authigenic silica in lacustrine shale and its hydrocarbon significance. Petrol. Explor. Dev. 49, 896–907.

Bai, X., Chen, R., Shang, F., Zhang, N., 2024. Sedimentary environment and oil-bearing characteristics of shale in Cretaceous Qingshankou Formation in Songliao Basin. Pet. Geol. Exp. 46, 1063–1074.

Brunauer, S., Deming, L.S., Deming, W.E., Teller, E., 1940. On a theory of the van der Waals adsorption of gases. J. Am. Chem. Soc. 62, 1723–1732.

Chang, J., Fan, X., Jiang, Z., Wang, X., Chen, L., Li, J., Zhu, L., Wan, C., Chen, Z., 2022. Differential impact of clay minerals and organic matter on pore structure and its fractal characteristics of marine and lacustrine shales in China. Appl. Clay Sci. 216, 106334.

Chen, L., Ji, H., Zhang, L., Jia, H., Zhu, Y., Fang, Z., 2017. Effect of burial processes on the evolution of organic acids and implications for acidic dissolution from a case study of the Nanpu Sag, Bohai Bay Basin, China. J. Nat. Gas Sci. Eng. 39, 173–187.

Curtis, J.B., 2002. Fractured shale-gas systems. AAPG Bull. 86, 1921–1938.

Du, J., Hu, S., Pang, Z., Lin, S., Hou, L., Zhu, R., 2019. The types, potentials and prospects of lacustrine shale oil in China. China Pet. Explor. 24, 560–568.

Feng, Y., Yang, Z., Jiang, W., Zhang, H., Zhang, T., Liu, C., Li, P., Zhu, J., Wang, X., 2024. The influence of mudstone lithofacies sedimentation on the development of shale oil "sweet-spot intervals" within large down-warped lacustrine basins in China. Mar. Petrol. Geol. 169, 107063.

Fu, J., Li, S., Niu, X., Deng, X., Zhou, X., 2020. Geological characteristics and exploration of shale oil in Chang 7 Member of Triassic Yanchang Formation, Ordos Basin, NW China. Petrol. Explor. Dev. 47, 870–883.

Fu, J., Li, S., Guo, Q., Guo, W., Zhou, X., Liu, J., 2022. Enrichment conditions and favorable area optimization of lacustrine shale oil in the Ordos Basin. Acta Petrol. Sin. 43, 1702–1716.

Han, W., Zhao, X., Jin, F., Pu, X., Chen, S., Mou, L., Zhang, W., Shi, Z., Wang, H., 2021. Sweet spots evaluation and exploration of lacustrine shale oil of the second member of Paleogene Kongdian Formation in Cangdong Sag, Bohai Bay Basin. Petrol. Explor. Dev. 48, 777–786.

Hart, B.S., Schieber, J., Kalinec, J., 2023. Clay diagenesis and overpressure development in Upper Cretaceous and tertiary shales of South Texas. Mar. Petrol. Geol. 147, 105978.

He, W., Cui, B., Wang, F., Wang, Y., Meng, Q., Zhang, J., Shao, H., Wang, R., Bai, Y., Lin, X., Zhao, Y., Sun, B., Fu, X., Xu, Q., Cui, K., Zhong, J., Gao, J., Sun, N., Mao, C., Shao, Z., Ni, L., Song, Q., Xue, C., Hao, B., Sheng, P., Zhang, J., Wang, Y., Zhang, W., 2022a. Study on reservoir spaces and oil states of the Cretaceous Qingshankou Formation in Gulong Sag, Songliao Basin. Geol. Rev. 68, 693–741.

He, W., Wang, M., Wang, X., Meng, Q., Wu, Y., Lin, T., Li, J., Zhang, J., 2022b. Pore structure characteristics and affecting factors of shale in the first member of the Qingshankou Formation in the Gulong Sag, Songliao Basin. ACS Omega 7, 35755–35773.

He, W., Wu, H., Yang, S., Wu, W., Li, N., Bai, Y., Wang, R., Zhao, Y., Qi, Y., Zhao, X., 2023a. Lithofacies division and type evaluation of shale oil reservoir in Fengcheng Formation of Mahu Sag, Junggar Basin. Northwest. Geol. 56, 217–231.

He, W., Yang, S., Wu, W., Li, N., Bai, Y., Wang, R., Zhao, Y., Qi, Y., Zhao, X., 2023b. Lithofacies division and type evaluation of shale oil reservoir in Fengcheng Formation of Mahu Sag, Junggar Basin. Northwest. Geol. 56, 217–231.

He, S., Tan, W., Li, H., Wang, Y., Niu, P., Qin, Q., 2025. Mineralogical and lithofacies controls on gas storage mechanisms in organic-rich marine shales. Energy Fuels 39 (8), 3846–3858.

Hu, T., Pang, X., Jiang, S., Wang, Q., Zheng, X., Ding, X., Zhao, Y., Zhu, C., Li, H., 2018. Oil content evaluation of lacustrine organic-rich shale with strong heterogeneity: a case study of the Middle Permian Lucaogou Formation in Jimusaer Sag, Junggar Basin, NW China. Fuel 221, 196–205.

Hu, S., Zhao, W., Hou, L., Yang, Z., Zhu, R., Wu, S., Bai, B., Jin, X., 2020. Development potential and technical strategy of lacustrine shale oil in China. Petrol. Explor. Dev. 47, 819–828.

Hu, T., Jiang, F., Pang, X., Liu, Y., Xu, T., Wu, G., Lv, J., Jiang, Z., Hu, Y., Li, C., Zhang, C., Hu, M., Huang, R., Wang, W., 2021. A Method and Device for Evaluating the Expelled Hydrocarbon and Exogenous Hydrocarbon Injection in Mud Shale: CN202110966591, vol. 8, 2021-11-26.

Hua, G., Wu, S., Qiu, Z., Jing, Z., Xu, J., Guan, M., 2021. Lamination texture and its effect on reservoir properties: a case study of Longmaxi Shale, Sichuan Basin. Acta Sedimentol. Sin. 39, 1–16.

Hua, G., Wu, S., Zhang, J., Liu, R., Guan, M., Cai, Y., Li, M., Zhang, S., 2022. Laminar structure and reservoir quality of shales with high clay mineral content in the Qingshankou Formation, Songliao Basin. Energies 15, 6132.

Huang, X., Wang, Z., He, M., Wu, K., Chen, L., Zuo, X., Xue, L., Liu, S., Hou, W., Li, X., Wang, Y., Lu, J., 2025. Influence of CO_2 injection on characterization of microscopic pore throat structure in shale reservoirs. Fuel 381, 133578.

Jin, L., Wang, G., Wang, Z., Chen, J., Pang, X., Wang, S., Zhou, Z., He, Z., Qin, Z., Fan, X., 2018. A review on pore structure characterization in tight sandstones. Earth Sci. Rev. 177, 436–457.

Jin, Z., Wang, G., Liu, G., Gao, B., Liu, Q., Wang, H., Liang, X., Wang, R., 2021. Research progress and key scientific issues of lacustrine shale oil in China. Acta Petrol. Sin. 42, 821–835.

Kuang, L., Hou, L., Yang, Z., Wu, S., 2021. Key parameters and methods of lacustrine shale oil reservoir characterization. Acta Pet. Sin. 42, 1–14.

Li, Y., Zhang, X., Lu, X., Cui, Y., Tang, Z., Wang, B., He, J., Huang, Z., 2013. Characteristics and validity analysis of hydrocarbon source rocks of upper Paleozoic in Songliao Basin. J. Earth Sci. Environ. 35, 39–48.

Li, S., Zhang, J., Gong, F., Zhu, H., Bai, Y., 2017. The characteristics of mudstones of Upper Cretaceous Qingshankou Formation and favorable area optimization of shale oil in the north of Songliao Basin. Geol. Bull. China 36, 654–663.

Li, W., Pang, X., Zhao, Z., Xu, Y., Zhang, K., 2018. Evaluation on the conventional and unconventional oil and gas resources in K1qn1 of Songliao Basin. China Offshore Oil Gas 30, 46–54.

Li, M., Ma, X., Jiang, Q., Li, Z., Pang, X., Zou, C., 2019. Enlightenment from formation conditions and enrichment characteristics of marine shale oil in North America. Pet. Geol. Recover. 26, 13–18.

Li, L., Bao, Z., Li, D., Li, Z., Ban, S., Li, Z., Wang, T., Li, Y., Zheng, N., Zhao, C., Chen, L., Chen, J., 2024. The source and preservation of lacustrine shale organic matter: insights from the Qingshankou Formation in the Changling Sag, Southern Songliao Basin, China. Sediment. Geol. 466, 106649.

Lin, S., Yuan, X., Yang, Z., 2017. Comparative study on lacustrine shale and mudstone and its significance: a case from the 7th member of Yanchang Formation in the Ordos Basin. Oil Gas Geol. 38, 517–523.

Liu, B., Shi, J., Fu, X., Lv, Y., Sun, X., Gong, L., Bai, Y., 2018. Petrological characteristics and shale oil enrichment of lacustrine fine-grained sedimentary system: a case study of organic-rich shale in the first member of Cretaceous Qingshankou Formation in Gulong Sag, Songliao Basin, NE China. Petrol. Explor. Dev. 45, 828–838.

Liu, B., Sun, J., Zhang, Y., He, J., Fu, X., Yang, L., Xing, J., Zhao, X., 2021. Reservoir space and enrichment model of shale oil in the first member of Cretaceous Qingshankou Formation in the Changling Sag, southern Songliao Basin, NE China. Petrol. Explor. Dev. 48, 521–535.

Liu, D., Yao, Y., Chang, Y., 2022. Measurement of adsorption phase densities with respect to different pressure: potential application for determination of free and adsorbed methane in coalbed methane reservoir. Chem. Eng. J. 446, 137103.
Liu, H., Li, Z., Bao, Y., Zhang, S., Wang, W., Wu, L., Wang, Y., Zhu, R., Fang, Z., Zhang, S., Liu, P., Wang, M., 2023. Geology of shales in prolific shale-oil well BYP5 in the Jiyang depression, Bohai Bay Basin. Oil Gas Geol. 44, 1405–1417.
Liu, X., Liu, J., Wang, X., Guo, Q., Lv, Q., Yang, Z., Zhang, Y., Zhang, Z., Zhang, W., 2025. Mechanisms of fine-grained sedimentation and reservoir characteristics of shale oil in lacustrine freshwater lacustrine basin: a case study from Chang 73 sub-member of Triassic Yanchang Formation in southwestern Ordos Basin, NW China. Petrol. Explor. Dev. 52, 84–88.
Lu, J., Zeng, H., Wang, Q., Feng, Z., Jiang, H., Wang, R., Li, B., Huo, Q., Sun, L., 2025. Phase behavior of nanoconfined continental shale oil and reservoir fluid phases in the Gulong shale of the Songliao basin. Sci. Rep. 15 (1), 16210.
Ma, Y., Cai, X., Zhao, P., Hu, Z., Liu, H., Gao, B., Wang, W., Li, Z., Zhang, Z., 2022. Geological characteristics and exploration practices of lacustrine shale oil in China. Acta Geol. Sin. 96, 155–171.
Pang, X., Mountney, N., Kuang, L., Zhao, X., Zhao, Y., Li, H., Han, Z., Tian, H., Wang, G., 2023a. Prediction of lamina structure and reservoir quality in shale using well logs: the Cretaceous Qingshankou Formation, Gulong Sag, Songliao Basin, China. Geoenergy Sci. Eng. 227, 211827.
Pang, X., Wang, G., Kuang, L., Zhao, F., Li, H., Han, Z., Bai, T., Lai, J., 2023b. Logging evaluation of lithofacies and their assemblage under control of sedimentary environment: a case study of the Qingshankou Formation in Gulong sag, Songliao Basin. J. Palaeogeogr. 25 (5), 1156–1175.
Peters, K., 1986. Guidelines for evaluating petroleum source rock using programmed pyrolysis. AAPG Bull. 70, 318–329.
Peters, K.E., Cassa, M.R., 1994. Applied source rock geochemistry. In: Magoon, L.B., Dow, W.G. (Eds.), The Petroleum System - from Source to Trap, vol. 4. AAPG Bull., Tulsa, pp. 93–120.
Pu, X., Dong, J., Chai, G., Song, S., Shi, Z., Han, W., Zhang, W., Xie, D., 2024. Enrichment model of high-abundance organic matter in shales in the 2nd member of the Paleogene Kongdian Formation, Cangdong Sag, Bohai Bay Basin. Oil Gas Geol. 45, 696–709.
Rexer, T.F., Mathia, E.J., Aplin, A.C., Thomas, K.M., 2014. High-pressure methane adsorption and characterization of pores in Posidonia shales and isolated kerogens. Energy Fuels 28, 2886–2901.
Sing, K.S.W., 1985. Reporting physisorption data for gas/solid systems with special reference to the determination of surface area and porosity. Pure Appl. Chem. 57 (4), 603–619.
Sun, M., Zhang, L., Hu, Q., Pan, Z., Yu, B., Sun, L., Bai, L., Fu, H., Zhang, Y., Zhang, C., Cheng, G., 2020. Multiscale connectivity characterization of marine shales in southern China by fluid intrusion, small-angle neutron scattering (SANS), and FIB-SEM. Mar. Petrol. Geol. 112, 104101.
Sun, L., Liu, H., He, W., Li, G., Zhang, S., Zhu, R., Jin, X., Meng, S., Jiang, H., 2021. An analysis of major scientific problems and research paths of Gulong shale oil in Daqing Oilfield, NE China. Petrol. Explor. Dev. 48, 453–463.
Sun, L., Zhu, R., Zhang, T., Cai, Y., Feng, Z., Bai, B., Jiang, H., Wang, B., 2024. Advances and trends of non-marine shale sedimentology: a case study from Gulong Shale of Daqing Oilfield, Songliao Basin, NE China. Petrol. Explor. Dev. 51 (6), 1183–1198.
Tang, Y., He, W., Jiang, Y., Fei, L., Dan, X., Zhao, Y., Zheng, M., Cao, J., Qin, Z., Yang, S., Wang, R., Zhu, T., Gao, G., 2023. Enrichment conditions and exploration direction of Permian saline lacustrine shale oil and gas in Junggar Basin. Acta Pet. Sin. 44, 5–43.
Tang, B., Meng, Q., Hu, F., Jiang, N., Yang, L., Xing, J., Liu, Z., Liu, Y., 2025. Orbital forcing on lacustrine shale deposition in the Late Cretaceous Songliao Basin, Northeastern China: responses and synergistic effects of organic matter sources, paleoenvironment, and seawater incursion events. Palaeogeogr. Palaeoclimatol. Palaeoecol. 676, 113133.
Thommes, M., Kaneko, K., Neimark, A.V., Olivier, J.P., Rodriguez-Reinoso, F., Rouquerol, J., Sing, K.S.W., 2015. Physisorption of gases, with special reference to the evaluation of surface area and pore size distribution (IUPAC Technical Report). Pure Appl. Chem. 87, 1051–1069.
Wan, J., Yu, Z., Yuan, Y., Sun, M., Huang, W., Rezaee, R., 2025. Laminae in multiple lithofacies and impact on pore structures in lacustrine shale: the cretaceous qingshankou formation, Songliao Basin. Mar. Petrol. Geol. 174, 107321.
Wang, H., Liu, Y., Wang, X., Liu, Z., Lv, D., Zhang, S., 2024. The source and sink process and its geological driving factors of shale organic matter in the Qingshankou Formation, Songliao Basin. Bull. China Soc. Mineral Petrol. Geochem. 43, 306–318.
Wang, T., Ji, W., Li, Y., Gong, F., 2025. Petrographic types and pore development characteristics of shales in the first member of Qingshankou Formation, Qijia-Gulong Sag, Songliao Basin. Chin. J. Geol. 60, 62–70.
Wu, J., Wang, H., Shi, Z., Wang, Q., Zhao, Q., Dong, D., Li, S., Liu, D., Sun, S., Qiu, Z., 2021. Favorable lithofacies types and genesis of marine-lacustrine transitional black shale: a case study of Permian Shanxi Formation in the eastern margin of Ordos Basin, NW China. Petrol. Explor. Dev. 48, 1137–1149.
Xiao, D., Li, Z., Wang, M., Dang, W., Xie, X., Han, B., 2025. A saturation model of lacustrine shale oil considering the influence of organic matter: a case study of the first member of the Cretaceous Qingshankou Formation of Changling Sag in southern Songliao Basin, NE China. Petrol. Explor. Dev. 52 (5), 1209–1221.
Xie, X., Amann-Hildenbrand, A., Littke, R., Krooss, B.M., Li, M., Li, Z., Huang, Z., 2019. The influence of partial hydrocarbon saturation on porosity and permeability in a Palaeogene lacustrine shale-hosted oil system of the Bohai Bay Basin, Eastern China. Int. J. Coal Geol. 207, 26–38.
Xiong, C., Chen, J.Y., Xu, R.N., Song, Q., 2025. Pyrolysis characteristics and mechanism of oil shale in the Songliao Basin of China. Fuel 386, 134251.
Xu, X., Liu, W., Bai, J., Chen, S., Li, Y., 2021. Enrichment characteristics and resource potential of shale oil in the first member of Qingshankou Formation in southern Songliao Basin. Geol. Resour. 30, 296–305.
Yawar, Z., Schieber, J., 2017. On the origin of silt laminae in laminated shales. Sediment. Geol. 360, 22–34.
Zhang, J., Xu, X., Bai, J., Chen, S., Liu, W., Li, Y., 2022a. Accumulation and exploration of continental shale gas resources of Cretaceous Shahezi Formation in Lishu fault depression, Songliao Basin, NE China. Petrol. Explor. Dev. 49 (3), 502–515.
Zhang, P., Misch, D., Meng, Q., Sachsenhofer, R.F., Liu, Z., Jia, J., Gao, F., Bechtel, A., Hu, F., 2022b. Lateral changes of organic matter preservation in the lacustrine Qingshankou Formation (Cretaceous Songliao Basin, NE China): evidence for basin segmentation. Int. J. Coal Geol. 254, 103984.
Zhang, H., Wang, X., Jia, C., Li, J., Meng, Q., Jiang, L., Wang, Y., Bai, X., Zheng, Q., 2023. Total petroleum system and hydrocarbon accumulation model in shallow and medium strata in northern Songliao Basin, NE China. Petrol. Explor. Dev. 50, 683–694.
Zhao, Z., Littke, R., Zieger, L., Hou, D., Froidl, F., 2020. Depositional environment, thermal maturity, and shale oil potential of the Cretaceous Qingshankou Formation in the eastern Changling Sag, Songliao Basin, China: an integrated organic and inorganic geochemistry approach. Int. J. Coal Geol. 232, 103621.
Zhao, X., Zhou, L., Pu, X., Jin, F., Han, W., Shi, Z., Chen, C., Jiang, W., Guan, Q., Xu, J., Liu, X., Zhang, W., Ma, J., 2022. Theories, technologies, and practices of lacustrine shale oil exploration and development: a case study of Paleogene Kongdian Formation in Cangdong sag, Bohai Bay Basin, China. Petrol. Explor. Dev. 49, 616–626.
Zheng, Y., Liao, Y., Wang, Y., Xiong, Y., Peng, P., 2018. Organic geochemical characteristics, mineralogy, petrophysical properties, and shale gas prospects of the Wufeng-Longmaxi shales in Sanquan Town of the Nanchuan District, Chongqing. AAPG Bull. 102, 2239–2265.
Zhi, D., Tang, Y., Yang, Z., Guo, X., Zheng, M., Wan, M., Huang, L., 2019. Geological characteristics and accumulation mechanism of lacustrine shale oil in Jimusaer sag, Junggar Basin. Oil Gas Geol. 40, 524–534.
Zou, C., Yang, Z., Zhu, R., Zhang, G., Hou, L., Wu, S., Tao, S., Yuan, X., Dong, D., Wang, Y., Wang, L., Huang, J., Wang, S., 2015. Progress in China's unconventional oil & gas exploration and development and theoretical technologies. Acta Geol. Sin. 89 (6), 979–1007.
Zou, C., Pan, S., Horsfield, B., Yang, Z., Hao, S., Liu, E., Zhang, L., 2019. Oil retention and intrasource migration in the organic-rich lacustrine Chang 7 shale of the Upper Triassic Yanchang Formation, Ordos Basin, central China. AAPG Bull. 103, 2627–2663.
Zou, C., Ma, F., Pan, S., Zhang, X., Wu, S., Fu, G., Wang, H., Yang, Z., 2023. Formation and distribution potential of global shale oil and the developments of lacustrine shale oil theory and technology in China. Earth Sci. Front. 30, 128–142.